Transmitted with letter dtd 6/22/98

Patterns of Ground Motion Amplitudes from Numerically Simulated Earthquakes[1]

Goodluck I. Ofoegbu[2], David A. Ferrill, Kevin J. Smart[3] and John A. Stamatakos

Center for Nuclear Waste Regulatory Analyses

Southwest Research Institute

6220 Culebra Road

San Antonio Texas 78238-5166

[1]Intended for publication in *Bulletin Seismological Society of America*: June 19, 1998, Draft

[2]Phone: (210)-5226641 Fax: (210)-5226081 e-mail: gofoegbu@swri.edu

[3]School of Geology and Geophysics, 100 East Boyd, University of Oklahoma, Norman, Oklahoma 73019

426.1

Abstract Results from a two-dimensional dynamic finite element model of normal-fault earthquakes indicate that the fault subsurface geometry has a strong effect on patterns of ground motion amplitudes. Seismic energy released by fault slip propagates radially from the hypocenter but is concentrated in discrete pulses that propagate horizontally and in directions normal and parallel to the fault. Because both the horizontal and fault-parallel pulses are largely dissipated and of relatively low intensity prior to reaching the ground surface, seismic motion at the ground surface is caused mainly by a single high-energy pulse that propagates along the upward fault normal from the hypocenter. Maximum ground motion occurs along the path of the normally directed high-energy pulse, which, for a homogeneous rock mass, is controlled by the subsurface fault geometry and hypocenter depth. For example, an earthquake caused by dip slip at a depth of 10 km on a 60° dipping fault would produce maximum surface motion on the hanging wall at about 12 km from the surface trace of the fault. This ground motion pattern, which results from the energy radiation characteristics associated with fault rupture, is significantly different from the pattern given by ground motion attenuation models. Such models, by design, give maximum ground motion at or near the surface trace of the causative fault. As a result, relationships based on traditional attenuation models may underestimate ground motion from normal-fault earthquakes in the maximum-motion area and overestimate it in areas near the surface trace of the fault. An attenuation model for normal fault earthquakes should account for the preferential propagation of seismic energy along the hypocentral normal as well as decreasing amplitudes with increasing distance from the hypocenter, in addition to other factors such as earthquake magnitude and site characteristics. The energy radiation pattern observed in the study also causes spatial variation of the relationship between subsurface and surface ground motion amplitudes. The ratio of subsurface to surface amplitudes may be much larger than 1.0 at sites within the travel path of the high energy pulse, because seismic energy arrives at such sites as direct body waves from the hypocenter. On the other hand, sites that are far

enough away from the high-energy pulse receive seismic energy through a combination of surface and body waves. Ground motion amplitudes may decrease with depth at such sites, but the ratio of subsurface to surface amplitudes remains larger than 0.5, a value commonly suggested for design of underground structures. Consequently, generalized application of a single reduction factor for the estimation of subsurface ground motion is not consistent with the expected ground motion patterns within the near field of normal-fault earthquakes.

Introduction

Predictions of ground accelerations in seismic hazard analyses are generally based on ground motion attenuation relationships that express ground motion as a function of earthquake magnitude, source-to-site distance, and other factors such as style of faulting (e.g., strike-slip or normal fault) and site conditions (i.e., depth of soil cover). Most ground motion attenuation relationships have been developed by fitting a function (often suggested by theory) to a set of strong ground motion data from previous earthquakes (e.g., Abrahamson and Shedlock, 1997). A majority of existing ground motion attenuation relationships have been derived from reverse and strike-slip earthquakes. Ground motion due to normal-fault earthquakes is generally estimated by applying a factor to results from other earthquake types (e.g., Campbell, 1997; Sadigh et al., 1997). Spudich et al. (1997) recently developed a relationship for earthquake ground motions in extensional tectonic regimes that is expected to apply equally to both strike-slip and normal-fault earthquakes under such tectonic conditions.

Although ground motion attenuation relationships derived from empirical ground motion data are generally reliable for far field ground accelerations, few measurements are available to evaluate the spatial pattern and amplitude of motion in the near field. For example, rupture-directivity effects (at sites that lie in the direction of rupture propagation compared to sites that lie in the opposing direction, relative to the hypocenter) cause spatial variations in near-field ground motion amplitudes and duration (Somerville et al., 1997). Sites that lie in the direction of rupture propagation experience increased ground-motion amplitudes whereas sites that lie away from the rupture-propagation direction experience smaller ground-motion amplitudes (e.g., Somerville et al., 1997). Rupture directivity also causes differences between

strike-normal and strike-parallel components of horizontal ground motion amplitudes in the near field. Rupture directivity effects may develop in association with either strike-slip or dip-slip faulting, including both reverse and normal faults, and are due to the fact that the propagation of rupture towards a site causes most of the seismic energy from the rupture to arrive in a single large pulse of motion oriented normal to the fault (Somerville et al., 1997). This preferential orientation of the energy pulse suggests that the subsurface geometry of a rupture surface may be an important factor controlling patterns of ground-motion amplitudes in the near field. For example, combined effects of rupture-surface geometry and sedimentary-basin morphology have been cited to explain certain differences between ground motion recorded in the Los Angeles basin (especially Santa Monica and West Los Angeles) and San Fernando Valley during the 1994 Northridge earthquake (Graves, 1995; Pitarka and Irikura, 1996).

Attenuation relationships are developed through regression of data from different earthquakes generated by a wide variety of fault geometries and rupture-propagation directions. As a result, specific attributes that may be important for defining near-field ground motion patterns may be averaged out as statistical variations. Somerville et al. (1997) developed modifications for empirical ground motion attenuation relations to account for the effects of rupture directivity on ground motion amplitudes and duration.

In the present study, we use two-dimensional (plane strain) dynamic finite element analyses to simulate normal-fault earthquakes (in vertical, fault-perpendicular profile) to study resulting patterns of ground acceleration. Because of the two-dimensional approximation, only in-plane motion components (i.e., vertical and strike-normal ground-motion components) and spatial patterns were examined. Furthermore, the use of a two-dimensional model precludes the consideration of three-dimensional effects, such as related to strike-parallel propagation of fault rupture or seismic waves. The results indicate that most of the seismic energy from a normal-fault earthquake arrives at the ground surface in a single pulse

that propagates along the upward fault normal from the hypocenter. This energy radiation pattern controls the pattern of ground motion. Areas traversed by the normally directed high-energy pulse experience relatively large ground motions. As a result, ground motion patterns calculated from the finite element model are significantly different from patterns calculated using traditional attenuation relationships that assume the occurrence of maximum ground motion at a location near the surface trace (or projection) of the causative fault. The finite element results indicate that attenuation models should account for the effects of fault geometry (i.e., concentration of seismic energy along the hypocentral normal) and source-to-site distance, in addition to other factors such as earthquake magnitude.

Finite Element Model

The modeled domain is a vertical dip section of a hypothetical normal fault that has a dip of 60° at the ground surface and flattens into a horizontal detachment at a depth of 12 km. The hanging wall is broken by two 75°-dipping antithetic faults, one terminating on the steep segment of the main fault, and the other on the horizontal segment. The faults are designated F0 (main fault), F1, and F2 (Fig. 1). This geometry is similar to the interpreted subsurface geometry of the Yucca Mountain region (Ferrill et al., 1996), which consists of an east-dipping normal fault (Bare Mountain Fault) that soles into a subhorizontal detachment at about 12 km depth with the hanging-wall block broken by a number of steeply dipping antithetic faults. The antithetic faults, F1 and F2, were found to have little effect on the analysis results and will, as a result, not be mentioned further.

Analyses were conducted using a two-dimensional (2D), plane strain, finite element model (Fig. 2) constituted from eight-noded quadrilateral elements with a few six-noded triangular elements added to facilitate mesh-density gradations. The plane strain model implies an assumption that the fault geometry does not vary in the strike direction and the horizontal component of deformation is normal to the strike. Such a model is suitable for the analysis of dip-slip faulting where the effects of along-strike variations of fault geometry and material properties can be ignored. Results obtained from such a model are applicable at points on or close to the modeled plane and become less applicable as the distance of a receiver location from the modeled plane increases.

Initial conditions consist of zero strain, vertical stress gradient of 25 MPa/km depth (based on constant density of 2500 kg/m^3 and gravitational acceleration of 10 m/s^2) and horizontal-to-vertical stress ratio $k_h = 0.25$. Boundary conditions are free-surface conditions

at the ground surface (top of model) and zero-perturbation conditions (no displacement normal to boundary) at the base and vertical boundaries (Fig. 1). The distance of the model base and vertical boundaries from the main fault was selected to ensure that energy generated at the fault would not reflect back from the boundaries within a simulation time of 10-12 s. To further reduce the possibility of interference due to reflected energy, a 1.5-km strip next to the base and vertical boundaries ("Absorbing Boundary" in Fig. 1) was assigned high damping properties to simulate the absorption of energy into the surrounding infinite domain.

The model domain was treated as homogeneous, except for differences in mechanical behavior between the fault zones and the surrounding rock. Mechanical behavior was simulated using two material models: a linear-elastic model for the hanging wall and footwall, with constant Young's modulus $E = 32.5$ GPa and Poisson's ratio $\nu = 0.25$); and an elastic-plastic model for fault zones. Each fault was modeled as a 100-m thick solid assigned elastic-plastic behavior based on the Drucker-Prager yield criterion (Drucker and Prager, 1952) and dilation-dependent inelastic strain potential (Ofoegbu and Curran, 1992; Ofoegbu and Ferrill, 1998). The material parameters for the plastic model are Drucker-Prager friction angle $\beta = 50°$, unconfined compressive strength $\sigma_c = 5$ MPa, and dilation angle $\varphi = 30°$, which, for plane strain conditions, are equivalent to a Mohr-Coulomb friction angle of 47° and cohesion of 2.7 MPa (Hibbit, Karlsson and Sorensen, Inc., 1994; Ofoegbu and Ferrill, 1998). Elastic parameters for the fault zones were assigned the same values as the surrounding rock, i.e., $E = 32.5$ GPa and $\nu = 0.25$.

Three values of material-damping factor were applied in the analyses (cf., Ofoegbu and Ferrill, 1998): 0.025 for the fault zones, 0.002 for the hanging wall and footwall, and 0.2 for the 1.5-km wide strip at the base and vertical boundaries of the model. The large value assigned to the boundary strip was applied to simulate the absorption of energy into the surrounding infinite domain.

Each earthquake simulation was conducted in two steps. First, an initial static equilibrium state was established under the influence of initial stress, gravitational forces, and boundary restraint. Second, fault slip was induced through the application of a shear-stress pulse of magnitude $f_s\tau$ over a selected segment of the main fault (F0), where τ is the shear-stress magnitude required for incipient slip under the prevailing stress condition. The value of the scale factor f_s varied linearly from 0.0 at time t_o, through 1.25 at time $t_o + 0.25$ s, to 0.95 at time $t_o + 0.5$ s, and was held constant at 0.95 thereafter, where t_o is time at the beginning of the load-application analysis step. Both the magnitude of f_s and its variation with time were chosen (somewhat arbitrarily) to cause slip instantaneously over the segment of fault F0 subjected to applied shear stress (three such segments are labeled "Seismic Sources" in Fig. 1). Thereafter slip propagated down-dip and up-dip along the fault as was dictated by the propagation of the energy pulse that was released into the system through the shear-stress application. Both the nucleation size (down-dip width of the fault segment over which shear-stress pulse was applied) and depth were varied as shown in Table 1.

This procedure of earthquake simulation differs from a procedure described in the literature (e.g., Tsai et al., 1990) that is based on integration of a prescribed unit solution (Green's function) over a prescribed source function to obtain a synthetic accelerogram. Acceleration time histories calculated with the current procedure result from the dynamic response of the medium to the induced fault slip, which depends only on the specified material model and boundary conditions.

Fault Rupture Parameters and Earthquake Magnitudes

Fault slip in our models initiated at the source point (hypocenter of simulated earthquake), i.e., midpoint of the fault segment over which the shear-stress pulse was applied, and propagated upward to the ground surface and down toward the detachment. Typically, slip at the hypocenter occurred rapidly at first and slowed with time. On the other hand, slip at the ground surface occurred somewhat more slowly after a lag time that depends on the hypocenter depth (Figs. 3, 4, and 5). Average rupture rates calculated using the lag time between the onset of slip at the hypocenter and at the ground surface and average slip rates based on change in slip magnitudes between consecutive observation times (Table 2) indicate that the simulated events satisfy classifications of earthquakes based on rupture rates (Beroza and Jordan, 1990) and slip rates (Sibson, 1986). Maximum slip occurred at the hypocenter (Fig. 6) and slip terminated at a down-dip fault width of 13.5-13.7 km, which, for the 60° fault, implies maximum rupture depth of about 12 km (the depth of the horizontal detachment). Fault displacement on F0 varies from meters on the steep segment to millimeters on the detachment segment (Fig. 6). Based on the comparison of slip rates on steep and low-angle segments of a listric fault from a previous study (e.g., Ofoegbu and Ferrill, 1998), the small amounts of slip on the detachment segment of F0 were probably aseismic and, consequently, were discounted in the evaluation of down-dip rupture width (DRW). Values of DRW were determined using a seismic-rupture tip that corresponds to the intersection of the sloping and horizontal sections of each fault-displacement profile (Fig. 6).

Moment magnitudes **M** of simulated earthquakes were estimated using the surface-displacement and rupture-width formulas of Wells and Coppersmith (1994) and the seismic-moment formula (Kanamori and Anderson, 1975; Hanks and Kanamori, 1979). In addition,

the mechanical energy necessary to produce the calculated fault-displacement distributions (Fig. 6), referred to hereafter as slip energy, **E**, was obtained as follows:

$$\mathbf{E} = \int_S \tau_f D_f ds \tag{1}$$

where the integration is performed over the fault surface, D_f is fault displacement, and τ_f is the shear stress required to cause slip under the prevailing stress state. The quantities D_f and τ_f are evaluated at nodal points on the hanging-wall surface of fault F0 (Fig. 1) and the integration (Eq. 1) was performed on the hanging wall using the trapezoidal rule. The resulting values of **E** (Table 3) imply two relationships among moment magnitudes of the simulated earthquakes. For sources at the same depth, a source with a larger nucleation size produced a larger earthquake. For sources with the same nucleation size, deeper sources produced larger earthquakes. Similar relationships between **M** and source nucleation size and depth were also indicated by values of **M** calculated using the empirical formulas (surface-displacement, rupture-width, and seismic-moment formulas), which gave values of **M** in the 6-7 range (Table 3).

Ground Motion Patterns

Contours of the acceleration resultant, A_r ($= \sqrt{A_1 A_1 + A_2 A_2}$, where A_1 and A_2 are horizontal and vertical accelerations, respectively), indicate that the simulated slip events caused release of discrete pulses of seismic energy that propagated away from the hypocenter in three directions: horizontally and normal and parallel to the fault (Fig. 7). The distance of the pulses from the hypocenter at times of 1.0 and 3.0 s indicate that the horizontal-propagating pulse consisted of p-wave whereas the along-normal and fault-parallel pulses consisted of s-wave, considering p- and s-wave velocities of 3.95 and 2.28 km/s (based on values of elastic parameters and density presented earlier). The pulses that propagated in

horizontal and fault-parallel directions dissipated faster than the pulses that propagated along the fault normal. For example, the maximum value of A_r for the DS20 case (deep source with 2-km nucleation size) at 3.0 s following the start of the seismic event is about 11.6 m/s^2 within the along-normal pulses and <2.14 m/s^2 at every other point (Fig. 7). Similarly, magnitudes of A_r at 5.0 s were much higher within the along-normal pulses (up to 5.8 m/s^2) than at any other point. Similar acceleration patterns were observed for all the other model cases [e.g., DS05 (deep source with 0.5-km nucleation size) on right column of Fig. 7]. This history of acceleration patterns indicates that seismic energy released by the simulated fault slip was concentrated in two (shear-wave) pulses that propagated away from the hypocenter in a direction normal to the fault, one traveling downward and the other upward. The pulse that travelled along the upward normal was responsible for most of the seismic energy that reached the ground surface (Fig. 7 for time of 5.0 s). The along-fault and horizontal pulses also conveyed energy to the ground surface but were largely dissipated and of relatively low intensity prior to reaching the surface.

The observation that seismic energy due to fault slip arrived at the ground surface in essentially a single pulse is consistent with an observation by Somerville et al. (1997) that most of the seismic energy from fault rupture arrives at the ground surface in a single large pulse of motion that often occurs at the beginning of strong-motion records. Somerville et al. (1997) explained that the energy radiation pattern of the shear dislocation on the fault causes this large pulse of motion to be oriented in the direction perpendicular to the fault. As a result, the concentration of energy in two pulses that propagate along the hypocentral fault normal, one downward and the other upward as illustrated in Fig. 7, is a phenomenological attribute of shear dislocation. We conducted analyses with three different nucleation sizes for sources at depths of 6 and 10 km (Table 1) and the results (e.g., Fig. 7) indicate that the observed radiation pattern is independent of the nucleation size.

Contours of horizontal and vertical accelerations follow the same pattern as contours of

the acceleration resultant (Fig. 8). In both cases, the wavefronts become circular after about 3 s, indicating radial attenuation from the hypocenter, but acceleration amplitudes at a given wavefront are nonuniform, indicating that attenuation from the hypocenter is not radially symmetric. Maximum accelerations occur within the energy pulse that propagates along the upward fault normal from the hypocenter. As Figs. 7 and 8 show, this pulse first hits the ground surface at a point P between the upward-normal exit point, N, and the epicenter (Fig. 9). Consequently, ground motion due to a normal-fault earthquake with hypocenter at H would attain maximum values at P.

Acceleration Histories

Acceleration histories were monitored at 181 points on the ground surface, i.e., at every finite element node at the top of the model (Fig. 2); and at several points along the upward normal from the hypocenter and along vertical lines at horizontal coordinates of 19, 25, 26, 29, 32, 35, and 39 km. Results for points along the vertical lines were used to develop depth profiles of peak acceleration presented later. Results for points on the ground surface and along the upward hypocentral normal (e.g., Fig. 10 and Fig. 11, respectively, from case DS20) indicate spatial patterns of the calculated acceleration time histories and frequencies. For the along-normal points both maximum acceleration and frequency content decrease as distance from the hypocenter increases. For example, the peak horizontal acceleration at an along-normal distance of 74.5 m is about 19 m/s^2 spread over frequencies of up to 25 Hz (with maximum energy in the 1-2 Hz range). On the other hand, the peak horizontal acceleration is less than 4 m/s^2, concentrated in frequencies less than 2 Hz, at an along-normal distance of about 9 km. For points on the ground surface, peak acceleration attains maximum value near a horizontal coordinate of about x=25 km and decreases as horizontal distance from this location increases; but the dominant frequencies remain essentially the same (about 0.3 - 2.0 Hz), increasing only slightly as x approaches 25 km from either side.

The occurrence of maximum peak horizontal acceleration at this location arises from the fact that the high-energy pulse for this model case (case DS20) contacted the ground surface at about x=25 km, i.e., point P in Fig. 9 corresponds approximately to x=25 km for the DS20 case (see x_p in Table 3).

These results indicate that the dominant frequencies of the induced ground motions vary from a maximum of about 30-40 Hz near the hypocenter to a minimum in the 0.3 - 2.0 Hz range at distances greater than about 10 km from the hypocenter. The fourier amplitude spectra for points on the ground surface (Fig. 10) indicates that ground motion occurred mainly in the 0.3 - 2.0 Hz range with essentially zero motion at frequencies greater than about 5 Hz. On the other hand, response spectra for shallow crustal earthquakes (e.g., Abrahamson and Silva, 1997; Campbell, 1997; Sadigh et al., 1997) typically show dominant frequencies in the range 5-10 Hz and significant ground motion at higher frequencies, up to 100 Hz. The fact that such high frequencies are not present in the finite element results may be related to differences between natural rock-failure processes and the failure process represented by the elastic-plastic material model applied in the analyses. Whereas the applied material model accounts for sliding on essentially smooth surfaces, natural rock failure includes more complicated processes, such as tensile failure and asperity crushing, that may generate energy over a large frequency range. The size of finite elements in the model may also limit the frequencies of calculated motions. Element dimensions in the model range from 100 m by 250 m near the faults to about 1 km by 2 km near the exterior boundaries (Fig. 2). Stick-slip phenomena (not represented in the model) may also account for the wide range of frequencies observed in strong motion records.

Profiles of Peak Horizontal Acceleration

Values of peak horizontal acceleration (a_{hp}), i.e., maximum absolute value of acceleration from each time-history record, demonstrate a decrease of acceleration amplitudes with

increasing distance from the hypocenter. In addition, the results (e.g., Fig. 12 from case DS20) indicate the rate of attenuation from the hypocenter is not radially symmetric. Acceleration amplitudes decrease more abruptly along the fault than along the upward fault normal, because of the concentration of seismic energy along the normal (Figs. 7 and 8).

This difference between profiles of peak acceleration along the fault and along the upward fault normal suggests that the attenuation of ground motion from normal-fault earthquakes may depend on the angle ϕ in addition to distance from the hypocenter, r_{hypo} (i.e., distance along path HS_h or HS_f in Fig. 9). Peak acceleration decreases with increasing r_{hypo} but increases as the hypocenter-to-site ray path (e.g., HS_h) approaches the upward normal HN. Consequently, the point of maximum acceleration on the ground surface is controlled by varying influences of attenuation from the hypocenter and from the high-energy pulse, which may be expressed through functions involving the parameters r_{hypo} and ϕ, and coincides with the location where the normally directed high-energy pulse first contacts the ground surface (Figs. 7 and 8), i.e., point P in Fig. 9.

Profiles of a_{hp} on the ground surface (Figs. 13, 14, and 15) illustrate that the point P lies between the epicenter and the exit point of the upward normal, i.e., $x_H < x_P < x_N$ (see Tables 1 and 3 for definition and values of x_H, x_P, and x_N). The case of a 2-km source at 1.5-km depth (SS20) produced two maxima of a_{hp} on the ground surface (Table 3 and Fig. 15): a 0.2-g maximum at 15.46 km caused by the upward-normal directed pulse and a 0.22-g maximum at 19.26 km that was caused by the horizontally directed pulse (e.g., Fig. 7). The latter pulse contacted the ground surface in all cases but was largely dissipated and of relatively low intensity. However, because of the shallow hypocentral depth of the SS20 case, the horizontally directed pulse was close enough to the surface to cause similar ground-motion amplitudes as the upward-normal pulse. As Figs. 13, 14, and 15 show, such irregularities in a_{hp} profiles are common. Examination of the acceleration contours (e.g., Figs. 7 and 8) suggests that irregular distribution of ground-motion amplitudes is due to different pulses

of seismic energy released from the hypocenter contacting the ground surface at different locations and causing local ground-motion maxima at such locations. The overall maximum ground motion, which occurred at the locations (x_P) given in Table 3 and illustrated in Figs. 13, 14, and 15, is caused by the high-energy pulse directed along the upward fault normal from the hypocenter.

Ground Motion Attenuation Relationships

The ground-surface profiles of peak horizontal acceleration from the finite element analyses were compared with profiles of (i) peak ground acceleration (PGA) and (ii) 2 Hz spectral acceleration (PSA) from four different ground motion attenuation relationships. The attenuation relationships (Campbell, 1997; Sadigh et al., 1997; Spudich et al., 1997; Abrahamson and Silva, 1997) were selected from a set of five relationships for shallow earthquakes in active tectonic regions that were included in a recent compilation of attenuation functions (Abrahamson and Shedlock, 1997). One of the five relationships, Boore et al. (1997), was not included because the authors indicated that their equations are not applicable to normal-fault earthquakes. The relationships give peak acceleration as a function of moment magnitude **M** and site-to-source distance with provisions to account for style of faulting and site conditions. The attenuation relationships were evaluated for **M**=7, but, because of uncertainties involved with the estimation of **M** for the simulated earthquakes, the calculated accelerations were normalized with respect to the maximum acceleration obtained from each relationship.

Two of the relationships (Campbell, 1997; Sadigh et al., 1997) provide estimates for both PGA and PSA, Spudich et al. (1997) provide PGA but not PSA, and Abrahamson and Silva (1997) give PSA estimates only. The PGA values represent high-frequency motion (about 100 Hz) that was not accounted for in the finite element model, whereas the 2 Hz spectral values represent low-frequency motion within the dominant frequencies observed in the finite

element model. Comparison of the finite element profiles with the PGA profiles helps to determine whether conclusions regarding ground-motion patterns based on the relatively low-frequency motions from the finite element model may be applicable to higher-frequency motions.

The attenuation relationships use different definitions of site-to-source distance (Fig. 9). Campbell (1997) uses r_{seis}, the closest distance to the seismogenic rupture surface, with the stipulation that the seismogenic depth, d_{seis}, should be at least 3 km. We used d_{seis}=3 km (for **M**=7), following recommendations by Campbell (1997). Site-to-source distance is defined as the closest distance to the rupture surface (r_{rup}) in the relationships of Sadigh et al. (1997) and Abrahamson and Silva (1997), and as the closest horizontal distance to the vertical projection of the rupture (r_{jb}) in Spudich et al. (1997). Since the finite element model represents a homogenous rock medium (except for the fault zones that were modeled as fractured rock), parameters consistent with rock medium ("hard rock" for Campbell's model and "soft rock" for the Sadigh et al. model) were applied in the calculations. The value of style-of-faulting factor in Campbell's model was set to 0.5 as recommended for normal-fault earthquakes (Campbell, 1997). Both the fault-type and site-class factors in the Abrahamson-Silva model were set to zero following recommendation in Abrahamson and Silva (1997).

The patterns of peak acceleration calculated using the attenuation relationships (Figs. 16 and 17) are different from the pattern obtained from the finite element model. The patterns of normalized 2-Hz PSA from the attenuation relationships are the same as the patterns of normalized PGA from the relationships, and both patterns differ in the same way from the finite element results. The attenuation relationships by design give maximum ground motion over a "source area", which varies with the definition of source-to-site distance applied in a particular relationship, and values of ground motion that decrease with increasing distance from the "source area". The "source area" coincides with the location on the

ground surface at which the site-to-source distance has a minimum value, i.e., at the surface trace of the fault for the Sadigh et al. (1997) and Abrahamson and Silva (1997) models, at the surface projection of the top of the seismogenic rupture (determined by d_{seis}) in the Campbell (1997) model, or within the surface projection of the rupture in the Spudich et al. (1997) model. However, as illustrated earlier using acceleration contours (Figs. 7 and 8) and profiles (Figs. 13, 14, and 15), the location of the maximum ground motion from a normal-fault earthquake is controlled by the concentration of seismic energy in a high-energy pulse directed along the upward fault normal from the hypocenter. Maximum ground motion occurs at the point P (Fig. 9) where the high-energy pulse first contacts the ground surface, which, for the DS20 and IS20 model cases (used for this comparison), is at a distance of about 12 and 9 km, respectively, to the east of the surface trace of the normal fault (Tables 1 and 3). As a result of this difference between ground-motion patterns predicted using the attenuation relationships and the pattern that results from the energy radiation attribute of normal-fault earthquakes (Figs. 16 and 17), the attenuation relationships may underestimate ground-motion amplitudes in the maximum-ground-motion area of normal fault earthquakes (area near point P in Fig. 9). Also for the same reason, the attenuation relationships may overestimate ground motion amplitudes in the area near the surface trace of the causative fault.

Attenuation Model Based on Fault Geometry and Hypocenter-to-Site Distance

Examination of ground-motion patterns calculated from the finite element models (e.g., Figs. 7 and 8) leads to the observation that attenuation relationships for normal-fault earthquakes should account for decrease in ground-motion amplitudes (i) with increasing distance from the hypocenter and (ii) as the hypocenter-to-site ray path (Fig. 9) departs from the upward fault normal from the hypocenter. Such a relationship may be expressed in terms of

the following function for a specific earthquake (i.e., constant **M**):

$$\gamma = \alpha_o + \alpha_r f(r_{\text{hypo}}) + \alpha_\phi g(\phi) + \alpha_{r\phi} f(r_{\text{hypo}}) g(\phi) + h_w \beta \tag{2}$$

where γ is a function of the ground-motion variable to be predicted, $f(r_{\text{hypo}})$ and $g(\phi)$ are functions of r_{hypo} and ϕ, respectively, β is a function that expresses the effects of differences between hanging wall and footwall with h_w=0 on the footwall and 1 on the hanging wall (e.g., Abrahamson and Silva, 1997), and α_i (with $i = o$, r, ϕ, or $r\phi$) are empirical parameters that may be evaluated by curve-fitting. This attenuation relationship was fit to the peak-horizontal acceleration profiles in Figs. 13 and 14 using a multiple regression model in S-PLUS (Statistical Sciences, 1993). Functions γ and $f(r_{\text{hypo}})$ were set to $\ln a_{hp}$ and $\ln r_{\text{hypo}}$ as is customary with existing attenuation models (e.g., Campbell, 1997; Sadigh et al., 1997). The function $g(\phi)$ was defined as follows:

$$g(\phi) = 1 - r_{\text{rup}}/r_{\text{hypo}} \tag{3}$$

With this expression, $g(\phi)$=0 at the upward-normal exit point, $g(\phi)$=1 at the surface trace of the fault, and $0 < g(\phi) < 1$ at other points on the ground surface. The value of β for each of the finite element model cases was determined using the discontinuity between footwall and hanging-wall a_{hp} values at the surface trace of the fault (e.g., Fig. 14), i.e., $\beta = \ln(a_{\text{hwall}}/a_{\text{fwall}})$ where a_{hwall} and a_{fwall} are values of a_{hp} on the hanging-wall and footwall sides, respectively.

Values of the parameters β and α_i (with $i = o$, r, ϕ, or $r\phi$) from the simulated earthquakes with hypocenter depth at 10 km and 6 km are given in Table 4 and appear to vary with earthquake magnitude (represented by slip energy **E**) and hypocenter depth. Comparison of the peak acceleration profile from Eq. (2) with the corresponding finite element results (e.g., Fig. 18) indicates that this attenuation model has the capability to predict essential aspects

of the acceleration profile from a normal-fault earthquake.

Effect of Depth on Ground Motion Amplitude

Observations that underground structures generally sustain less damage from earthquakes than surface structures at the same geographic location (e.g., Owen and Scholl, 1981; Stepp, 1997), as well as empirical ground-motion data from a few down-hole strong motion arrays (e.g., King, 1982; Komada, 1991), have been interpreted to imply that ground motion from earthquakes generally decrease with depth (e.g., U.S. Department of Energy, 1997). Decrease in ground motion with depth may result from near-surface amplification due to either additive interaction of incident and reflected waves (e.g., Owen and Scholl, 1981) or upward decrease of shear wave velocity near the ground surface (e.g., Komada, 1991; Stepp, 1997). Ground-motion attenuation with depth may also be caused by the fact that the amplitude of Rayleigh waves decreases with depth (e.g., Richart et al., 1970).

Amplification due to additive interaction of multiply reflected waves may occur in soil layers overlying bedrock, where the fraction of seismic energy that enters the soil layers may become trapped because of reflections at the free surface and at the soil-bedrock interface (e.g., Stepp, 1997). Also, decrease in shear wave velocity towards the ground surface (because of decreasing effective confining pressure) in deep soil layers may result in ground motion increasing towards the surface because of the conservation of seismic-energy flux (e.g., Stepp, 1997). Both processes may occur at the same time and may account for the majority of empirical strong-motion data that indicate decrease in ground motion with depth at sites underlain by deep soil or layered soil over bedrock (e.g., Kanai et al., 1966; Owen and Scholl, 1981; Komada, 1991).

For rock sites, decrease of earthquake-induced ground motion with depth may occur if seismic energy arrives at a site mainly as surface waves. Reflection at the ground surface and interactions between the incident and reflected waves may also cause near-surface amplifi-

cation at rock sites, but the effects of this process on the variation of ground motion with depth can be exaggerated by models that assume full reflection of body waves at the ground surface (e.g., Owen and Scholl, 1981). Results from such models suggest that additive interactions of the incident and reflected waves lead to magnification by a factor that decreases from a maximum of about 2.0 at the ground surface to about 1.0 (i.e., no magnification) at a certain critical depth (e.g., Owen and Scholl, 1981). As a result, ground-motion amplitudes at and below such critical depth would be about half the amplitude at the ground surface. One problem with such models is that seismic energy incident at the ground surface is not fully reflected but is partitioned into surface waves and reflected (body) waves, with a greater fraction of energy going to surface waves (e.g., Richart et al., 1970). As a result, the magnification of surface ground motion relative to subsurface ground motion below the critical depth is likely to be much smaller than such models suggest.

Depth profiles of normalized peak horizontal acceleration calculated from the DS20 model case (Fig. 19) suggest the following for a homogeneous-rock site: (1) for hanging-wall sites at distance of about 13 km or less, or about 22 km or more, from the surface trace of the fault (i.e., at $x \leq 26$ or $x \geq 35$ km), subsurface peak horizontal acceleration is generally less than the corresponding value at the ground surface by a factor that lies between 0.5 and 1.0 with a value of about 0.75 being more likely; (2) for hanging-wall sites between distance of about 13 and about 22 km from the surface trace of the fault (i.e., $26 \leq x \leq 35$ km), subsurface peak horizontal acceleration generally exceeds the corresponding value at the ground surface by a factor of up to 2.0.

Comparison of peak-acceleration profiles at the ground surface and at 300-m depth from the finite element models (Figs. 13, 14, and 15) also indicate similar spatial variation of the relationship between surface and subsurface ground-motion amplitudes at a homogeneous rock site. For the cases with hypocenter depth at 6 km (Fig. 13), acceleration amplitudes at 300-m depth exceed the amplitudes at the ground surface for sites between x=21 and x=26

km, which correspond approximately to areas between points P and N in Fig. 9 for these cases (compare with x_P and x_N in Tables 3 and 1). Similarly, for cases with hypocenter at 10-km depth (Fig. 14), 300-m-depth accelerations exceed ground-surface accelerations at sites between x=25 and x=33 km, i.e, at locations between points P and N in these cases.

Locations between points P and N (Fig. 9), which correspond to horizontal coordinates between x_P and x_N (Tables 3 and 1), lie within the travel path of the normally directed high-energy pulse. Ground-motion amplitudes at such locations decrease with increasing distance from the hypocenter (irrespective of depth), following curves similar to the along-normal curve in Fig. 12. As a result, subsurface sites that fall within the travel path of the high-energy pulse experience higher-amplitude ground motions than ground-surface sites at corresponding horizontal location. At sites outside of the travel path, the amplitude of subsurface motion may be smaller or larger than at the ground surface because such sites receive seismic energy through a combination of surface waves and body waves.

These results (Figs. 13, 14, 15, and 19) suggest why values of subsurface-to-surface ground-motion ratio calculated based on empirical observation at a single site (e.g., Anderson et al., 1993) may not be generally applicable for estimating amplitudes of subsurface ground motion. The notion that ground motion from earthquakes generally decreases with depth has lead to suggestions that subsurface ground motion for underground engineering design may be estimated through reduction of surface ground motion (e.g., U.S. Department of Energy, 1994; U.S. Department of Energy, 1997). Such a procedure may be justified for sites overlain by deep soil or layered soil over bedrock, considering empirical data available for such sites (e.g., Kanai et al., 1966; Owen and Scholl, 1981; Komada, 1991). For rock sites, results presented in Figs. 13, 14, 15, and 19 agree with results from earlier analyses (Ofoegbu and Ferrill, 1998) and with observations from previous earthquakes (e.g., Kanai et al., 1966; Owen and Scholl, 1981), which indicate that subsurface ground motion may be larger than, equal to, or smaller than surface ground motion. The location of a site relative

to the seismic-energy travel path from the earthquake hypocenter to the ground surface, which depends on the causative-fault geometry and hypocenter depth, appears to be the factor that determines whether subsurface ground motion is smaller or larger than surface ground motion.

Conclusions

The subsurface geometry of normal faults has a strong effect on ground motion patterns from a normal-fault earthquake because of the energy radiation characteristics associated with fault rupture. Seismic energy released by fault slip consists of discrete pulses that propagate through the surrounding rock horizontally and in directions normal and parallel to the fault. Both the horizontal and fault-parallel pulses may reach the ground surface but are largely dissipated and of relatively low intensity prior to reaching the ground surface. Seismic motion at the ground surface is caused mainly by a single high-energy pulse that propagates along the upward fault normal from the hypocenter. Maximum ground motion (at the ground surface) resulting from the earthquake occurs at the location where this high-energy pulse first contacts the ground surface, which is controlled mainly by the subsurface fault geometry and hypocenter depth.

Existing ground motion attenuation relationships are designed to give maximum ground motion over a "source area" that varies with the definition of source-to-site distance applied in a particular relationship but is usually close to the surface trace of the causative fault. Results from the present study indicate that such location for maximum ground motion may be significantly offset from the location of maximum motion consistent with the energy radiation characteristics of normal-fault earthquakes. As a result, traditional attenuation models may underestimate the ground motion in the maximum-motion area of a normal-fault earthquake but overestimate the ground motion near the surface trace of the fault. Based on the interpretation of the analysis results presented in this paper it is suggested that an attenuation model for normal-fault earthquakes should account for decrease in ground motion as (i) the hypocenter-to-site distance increases and (ii) as the hypocenter-to-site ray

path departs from the upward fault normal (in addition to other factors, such as earthquake magnitude and site characteristics).

A general decrease of ground-motion amplitudes with depth below the ground surface is commonly applied to determine ground-motion inputs into engineering design of underground structures. Such a model has been interpreted from limited empirical data (mostly from sites underlain by deep soil or layered soil over bedrock), observations that underground structures often sustain less damage from earthquakes than surface structures, and theoretical models that assume full reflection of body waves at the ground surface such that interaction of the incident and reflected waves produce near-surface magnification that decreases with depth. Results from the current study indicate that, at sites underlain by homogeneous bedrock, the relationship between subsurface and surface ground-motion amplitudes varies spatially depending on location relative to the travel path of seismic energy from the hypocenter to the ground surface. For sites that lie within the travel path of the normally directed high-energy pulse responsible for most of the seismic energy that impacts the ground surface from a given earthquake, ground motion amplitudes decrease with increasing distance from the hypocenter, irrespective of depth. Ground motion amplitudes at a given depth with such sites may be as large as twice the amplitude at a corresponding ground-surface location. Sites that are far enough away from the high-energy pulse travel path receive energy more through surface waves than body waves. As a result, the amplitudes of ground motion at such sites may decrease with depth, but the ratio of subsurface to surface amplitudes remains much larger than the value of 0.5 that is often suggested for underground rock engineering. Consequently, the application of a general reduction factor to ground-motion estimates from attenuation relationships in order to obtain ground-motion inputs into engineering design of underground structures is not consistent with the energy-radiation characteristics associated earthquake-induced ground motion.

Acknowledgements

The work described in this paper was performed at the Center for Nuclear Waste Regulatory Analyses (Southwest Research Institute, San Antonio, Texas) for the United States Nuclear Regulatory Commission (NRC) under contract number NRC-02-93-005. The work was done on behalf of the NRC Office of Nuclear Material Safety and Safeguards, Division of Waste Management. The views expressed in the paper are those of the authors and do not necessarily reflect the views or regulatory position of the NRC. The authors are grateful to M.W. McCann, F. Tajima, S.M. Hsiung, H.L. McKague, and B. Sagar for valuable comments on the manuscript.

References

Abrahamson, N. A. and K. M. Shedlock (1997). Overview. *Seismological Research Letters* **68**(1), 9–23.

Abrahamson, N. A. and W. J. Silva (1997). Empirical response spectral attenuation relations for shallow crustal earthquakes. *Seismological Research Letters* **68**(1), 94–127.

Anderson, J. G., J. N. Brune, D. dePolo, J. Gomberg, S. C. Harmsen, M. K. Savage, A. F. Sheehan, and K. D. Smith (1993). Preliminary report: The Little Skull Mountain earthquake, June 29, 1992. In Q. A. Hasten (Ed.), *Dynamic analysis and design considerations for high level nuclear waste repositories*, pp. 162–175. American Society of Civil Engineers.

Beroza, G. C. and T. H. Jordan (1990). Searching for slow and silent earthquakes using free oscillations. *J. Geophys. Res.* **95**(B3), 2485–2510.

Boore, D. M., W. B. Joyner, and T. E. Fumal (1997). Equations for estimating horizontal response spectra and peak acceleration from Western North American earthquakes: A summary of recent work. *Seismological Research Letters* **68**(1), 128–153.

Campbell, K. W. (1997). Empirical near-source attenuation relationships for horizontal and vertical components of peak ground acceleration, peak ground velocity, and pseudo-absolute acceleration response spectra. *Seismological Research Letters* **68**(1), 154–179.

Drucker, D. C. and W. Prager (1952). Soil mechanics and plastic analysis of limit design. *Quart Appl Math* **10**(2), 157–172.

Ferrill, D. A., G. L. Stirewalt, D. B. Henderson, J. A. Stamatakos, A. P. Morris, B. P. Wernicke, and K. Spivey (1996). Faulting in the Yucca Mountain Region: Critical review and analyses of tectonic data from the Central Basin and Range. NUREG/CR–

6401, U.S. Nuclear Regulatory Commission, Washington, DC.

Graves, R. W. (1995). Preliminary analysis of long-period response in the Los Angeles region from the 1994 Northridge earthquake. *Geophysical Research Letters* **22**, 101–104.

Hanks, T. C. and H. Kanamori (1979). A moment magnitude scale. *J. Geophys. Res.* **84**, 2348–2350.

Hibbit, Karlsson and Sorensen, Inc. (1994). ABAQUS Users' Manual, Version 5.4. Pawtucket, RI: Hibbit, Karlsson and Sorensen, Inc.

Kanai, K., T. Tanaka, S. Yoshizawa, T. Morishita, K. Osada, and T. Suzuki (1966). Comparative studies of earthquake motions on the ground and underground II. *Bull. Earthquake Res. Inst.* **44**, 609–643.

Kanamori, H. and D. L. Anderson (1975). Theoretical basis of some empirical relations in seismology. *Bull. Seism. Soc. Am.* **65**, 1073–1095.

King, K. W. (1982). A study of surface and subsurface ground motions at Calico Hills, Nevada test site. Open-File Report 82-1044, U.S. Geological Survey.

Komada, H. (1991). Study on earthquake resistance of large underground caverns. In K. Hitoshi (Ed.), *Rock mechanics in Japan*, Volume VI, pp. 120–124. Japanese Committee for International Society for Rock Mechanics.

Ofoegbu, G. I. and J. H. Curran (1992). Deformability of intact rock. *Int. J. Rock. Mech. Min. Sci. & Geomech. Abstr.* **29**(1), 35–48.

Ofoegbu, G. I. and D. A. Ferrill (1998). Mechanical analyses of listric normal faulting with emphasis on seismicity assessment. *Tectonophysics* **284**, 65–77.

Owen, G. N. and R. E. Scholl (1981). Earthquake engineering of large underground structures. FHWA/RD-80/195, Federal Highway Administration, Washington, DC.

Pitarka, A. and K. Irikura (1996). Basin structure effects on long period strong motions in the San Fernando valley and the Los Angeles Basin from the 1994 Northridge earthquake and an aftershock. *Bulletin Seismological Society of America* **86**, S126–S137.

Richart, F. E., R. D. Woods, and J. R. Hall (1970). Vibrations of Soils and Foundations. Englewood Cliffs, NJ: Prentice-Hall.

Sadigh, K., C. Y. Chang, J. A. Egan, F. Makdisi, and R. R. Youngs (1997). Attenuation relationships for shallow crustal earthquakes based on California strong motion data. *Seismological Research Letters* **68**(1), 180–189.

Sibson, R. H. (1986). Earthquakes and rock deformation in crustal fault zones. *Ann. Rev. Earth Planet. Sci.* **14**, 149–175.

Somerville, P. G., N. F. Smith, R. W. Graves, and N. A. Abrahamson (1997). Modification of empirical strong ground motion attenuation relations to include the amplitude and duration effects of rupture directivity. *Seismological Research Letters* **68**(1), 199–222.

Spudich, P., J. B. Fletcher, M. Hellweg, J. Boatwright, C. Sullivan, W. B. Joyner, T. C. Hanks, D. M. Boore, A. McGarr, L. M. Baker, and A. G. Lindh (1997). SEA96—A new predictive relation for earthquake ground motions in extensional tectonic regimes. *Seismological Research Letters* **68**(1), 190–198.

Statistical Sciences (1993). S-PLUS guide to statistical and mathematical analysis, Version 3.2. Seattle: StatSci, a division of MathSoft, Inc.

Stepp, J. C. (Ed.) (1997). Seismic and dynamic analysis and design considerations for high level nuclear waste repositories. New York, NY: American Society of Civil Engineers.

Tsai, Y. B., F. W. Brady, and L. S. Cluff (1990). An integrated approach for characterization of ground motions in PG&G's long term seismic program for Diablo Canyon. In *Proceedings of 4th U.S. National Conference on Earthquake Engineering*, Volume 1, pp. 597–606.

U.S. Department of Energy (1994). Seismic design inputs for the Exploratory Studies Facility at Yucca Mountain. BAB000000-01717-5705-00001 REV00, U.S. Department of Energy Yucca Mountain Site Characterization Project Office, Las Vegas, NV.

U.S. Department of Energy (1997). Methodology to assess fault displacement and vibratory ground motion hazards at Yucca Mountain. Topical Report YMP/TR-002-NP, U.S. Department of Energy Office of Civilian Radioactive Waste Management, Las Vegas, NV.

Wells, D. L. and K. J. Coppersmith (1994). New empirical relationships among magnitude, rupture length, rupture width, rupture area, and surface displacement. *Bull. Seism. Soc. Am.* **84**, 974–1002.

Table 1: Source characteristics and fault displacements for simulated earthquakes

Model ID[1]	Depth[2] (km)	Size[3] (km)	$(x_H)^4$ (km)	$(x_N)^5$ (km)	$(D_s)^6$ (m)	$(D_{\max})^7$ (m)	$(D_{\text{avg}})^8$ (m)	(DRW)[9] (km)
SS20	1.5	2.0	13.9	16.5	3.16	4.23	1.89	13.5
IS05	6	0.5	16.5	26.9	0.95	4.27	1.48	13.7
IS10	6	1.0	16.5	26.9	2.03	6.90	2.91	13.7
IS20	6	2.0	16.5	26.9	4.12	11.6	5.76	13.7
DS05	10	0.5	18.8	36.1	0.5	5.35	1.38	13.7
DS10	10	1.0	18.8	36.1	1.18	8.61	2.84	13.7
DS20	10	2.0	18.8	36.1	2.39	13.9	5.59	13.7

[1] SS, IS, and DS stand for "shallow source", "intermediate source", and "deep source", respectively; numbers 05, 10, and 20, divided by 10, represent the nucleation size in km.

[2] Nucleation depth, i.e., depth of midpoint of fault segment over which shear-stress pulse was applied.

[3] Nucleation size, i.e., down-dip width of fault segment over which shear-stress pulse was applied.

[4] Horizontal coordinate of hypocenter relative to west boundary of model.

[5] Horizontal coordinate of surface intersection of upward fault normal from the hypocenter.

[6] Fault displacement at the ground surface.

[7] Maximum fault displacement.

[8] Average fault displacement.

[9] Down-dip rupture width.

Table 2: Slip and rupture rates on fault F0 from simulated earthquakes

Model	Slip Rate (m/s)		Average Rupture
ID	At Hypocenter	At Ground Surface	Rate (km/s)
SS20	0.08-1.5	0.02-0.48	2.31
IS05	0.04-3.0	0.01-0.16	1.73
IS10	0.05-3.4	0.09-0.29	2.31
IS20	0.1-5.0	0.11-0.58	3.46
DS05	0.03-3.8	0.03-0.10	2.89
DS10	0.02-4.4	0.07-0.14	3.30
DS20	0.1-7.7	0.13-0.30	3.85

Table 3: Moment magnitudes and ground acceleration from simulated earthquakes

Model	Moment magnitude from			$(a_{hpmax})^4$ (g) at		$(x_P)^5$	Slip energy[6]
ID	(SDM)[1]	(DRW)[2]	$(M_o)^3$	surface	300-m depth	(km)	(10^6 MJ/m)
SS20	7.0	6.4	6.3–6.7	0.20/0.22	0.20	15.46/19.26	1.162
IS05	6.6	6.4	6.3–6.6	0.18	0.16	19.26	1.428
IS10	6.8	6.4	6.5–6.8	0.31	0.30	19.26	2.736
IS20	7.0	6.4	6.7–7.0	0.37	0.38	21.75	5.421
DS05	6.4	6.4	6.3–6.6	0.22	0.19	24.75	1.791
DS10	6.7	6.4	6.5–6.8	0.39	0.39	24.94	3.607
DS20	6.9	6.4	6.7–7.0	0.55	0.60	24.94	7.094

[1] Moment magnitude from surface-displacement formula with values of D_s in Table 1.

[2] Moment magnitude from rupture-width formula with values of DRW in Table 1.

[3] Moment magnitude from seismic-moment formula with rupture area as L×DRW where rupture length, L, ranges from 0.8(DRW) to 2.5(DRW).

[4] Peak horizontal acceleration at ground surface and 300-m depth from finite element model.

[5] Horizontal coordinate of point of a_{hpmax} on the ground surface, i.e., point P in Fig. 9.

[6] Mechanical energy (per unit strike length) necessary to produce the calculated fault-displacement distributions (e.g., Fig. 6) under the prevailing stress state.

Table 4: Attenuation model parameters for simulated earthquakes

Model ID	β	α_o	α_r	α_ϕ	$\alpha_{r\phi}$
DS20	0.5216	3.4022	-1.8215	-14.086	5.0240
DS10	0.0429	4.4719	-2.2125	-10.844	3.8215
DS05	0.0189	4.4624	-2.4192	-9.9868	3.5522
IS20	0.6816	0.2722	-0.9880	-7.5411	3.3181
IS10	0.3868	1.3105	-1.4957	-5.9546	2.7173
IS05	0.2211	0.7855	-1.4517	-2.7858	1.3364

Parameters β, α_o, α_r, α_ϕ, and $\alpha_{r\phi}$ are defined in Eq. (2).

List of Figure Captions

1 Schematic illustration of finite element model. Rollers represent zero normal displacement boundary condition. White lines labeled F0, F1, and F2 represent faults, and red line segments represent fault segments subjected to shear-stress pulse (one at a time) to generate fault slip. Light-blue zone labeled "Absorbing Boundary" was assigned high-damping coefficient to simulate absorption of dynamic energy into infinite region around model domain.

2 Finite element discretization of the problem domain. The elements are eight-noded plane strain quadrilaterals with a few six-noded triangles added to facilitate mesh-density transitions. The bottom figure shows the entire model whereas the top figure is an enlargement of the area close to the faults.

3 Slip histories on F0 at the ground surface and at the hypocenter produced by sources at 10-km depth. The nucleation size for each source (0.5, 1.0, or 2.0 km) is indicated in the figure legend.

4 Slip histories on F0 at the ground surface and at the hypocenter produced by sources at 6-km depth. The nucleation size for each source (0.5, 1.0, or 2.0 km) is indicated in the figure legend.

5 Slip histories on F0 at the ground surface and at the hypocenter produced by a source at 1.5-km depth.

6 Profiles of fault displacement along F0 associated with simulated earthquakes of varying nucleation size and hypocenter depth. The seismic-rupture tips determined from these profiles indicate values of down-dip rupture width (DRW) of about 14 km (Table 1).

7 Patterns of acceleration resultant, A_r (m/s^2), at 1.0, 3.0, and 5.0 s following start of seismic event. $A_r = \sqrt{A_1 A_1 + A_2 A_2}$, where A_1 and A_2 are horizontal and vertical accelerations, respectively. The left-column figures are from Case DS20 (2-km source at 10-km depth) whereas the right-column figures are from Case DS05 (0.5-km source at 10-km depth). White lines labeled F0, F1 and F2 represent faults and the black line segment on F0 represents the seismic-source location. Notice that the radiation pattern appears insensitive to nucleation size (both the 2-km and 0.5-km sources give essentially the same pattern) but ground-motion magnitudes are highly sensitive to nucleation size. Maximum values of A_r range from 21.3 to 5.81 m/s^2 (2.17-0.59 g) for the DS20 case and 6.74-2.45 m/s^2 (0.69-0.25 g) for the DS05 case.

8 Patterns of horizontal and vertical acceleration, A_1 and A_2, respectively (m/s^2) at 1.0, 3.0, and 5.0 s following start of seismic event. Figures are from Case DS20 (2-km source at 10-km depth). The left-column figures show horizontal acceleration while the right-column figures show vertical acceleration. White lines labeled F0, F1 and F2 represent faults and the black line segment on F0 represents the seismic-source location.

9 (a) Schematic illustration of location of ground-motion maximum (point P) due to normal-fault earthquake with hypocenter at H and epicenter at E. The upward fault normal from the hypocenter intersects the ground surface at N. Point F represents the surface trace of the fault and S_f and S_h are typical instrument sites on the footwall and hanging wall, respectively. Site-to-fault distance r_{rup} is equal to OS_h on the hanging wall and FS_f on the footwall. Angle ϕ is the zenith angle between the fault plane and hypocenter-to-site ray path (e.g., Somerville et al., 1997). Figures (b) and (c) [from Abrahamson and Shedlock (1997)] illustrate the definitions of site-to-source distance measures employed in published attenuation relationships.

10 Histories of horizontal acceleration for points on the ground surface from analysis case DS20 (2-km source at 10-km depth). Number inside each plot box represents distance (km) from the west (left) boundary of the model. The hanging-wall surface of fault F0, epicenter of the simulated earthquake, and exit point of the upward fault normal are at distances of 13.05, 18.8, and 36.1 km, respectively, from the west boundary (Tables 1 and 3). The figures show that maximum ground motion and frequency content occur at a distance of about 25 km (i.e., between the upward-normal exit point and the epicenter).

11 Histories of horizontal acceleration for points on the upward fault normal from the hypocenter from analysis case DS20 (2-km source at 10-km depth). Number inside each plot box represents distance (km) from the hypocenter along the normal. The figures show that both acceleration magnitude and frequency content decrease with increasing distance from the hypocenter.

12 Profiles of peak horizontal acceleration up dip along the fault (on the hanging-wall side) and along the upward normal from the hypocenter, from model case DS20 (2-km source at 10-km depth). Both curves illustrate attenuation with distance from the hypocenter with a greater rate of attenuation along the fault than along the upward normal. The along-normal curve was based on points located within 100 m of the upward-normal path, which may explain the curve's waviness.

13 Profiles of peak horizontal acceleration on the ground surface and at 300-m depth produced by sources at 6 km depth, illustrating the effects of nucleation size on ground acceleration. Bottom figure shows fault geometry, source location (white line segment on fault), and outline of the model domain (compare with Fig. 1).

14 Profiles of peak horizontal acceleration on the ground surface and at 300-m depth produced by sources at 10 km depth, illustrating the effects of nucleation size on ground acceleration. Bottom figure shows fault geometry, source location (white line segment on fault), and outline of the model domain (compare with Fig. 1).

15 Profiles of peak horizontal acceleration on the ground surface and at 300-m depth produced by 2-km sources at depths of 1.5, 6, and 10 km, illustrating the effects of nucleation depth on ground acceleration. Bottom figure shows fault geometry, source location (white line segment on fault), and outline of the model domain (compare with Fig. 1).

16 Profiles of normalized peak spectral acceleration at 2 Hz from three attenuation relationships compared with the profile of peak horizontal acceleration from the finite element model cases DS20, i.e., 2-km source at 10-km depth (a), and IS20, i.e., 2-km source at 6-km depth (b). Accelerations were normalized with respect to the maximum value obtained from each relationship (or model).

17 Profiles of normalized peak ground acceleration from three attenuation relationships compared with the profile of peak horizontal acceleration from the finite element model cases DS20, i.e., 2-km source at 10-km depth (a), and IS20, i.e., 2-km source at 6-km depth (b). Accelerations were normalized with respect to the maximum value obtained from each relationship (or model).

18 Peak horizontal acceleration from finite element model case DS20 compared with profile calculated using Eq. (2) attenuation relationship with DS20 parameters (Table 4).

19 Depth profiles of normalized peak horizontal acceleration from finite element model case DS20. Numbers with arrows indicate the horizontal coordinate for each profile. Acceleration values were normalized with respect to the peak horizontal acceleration at the ground surface on each profile.

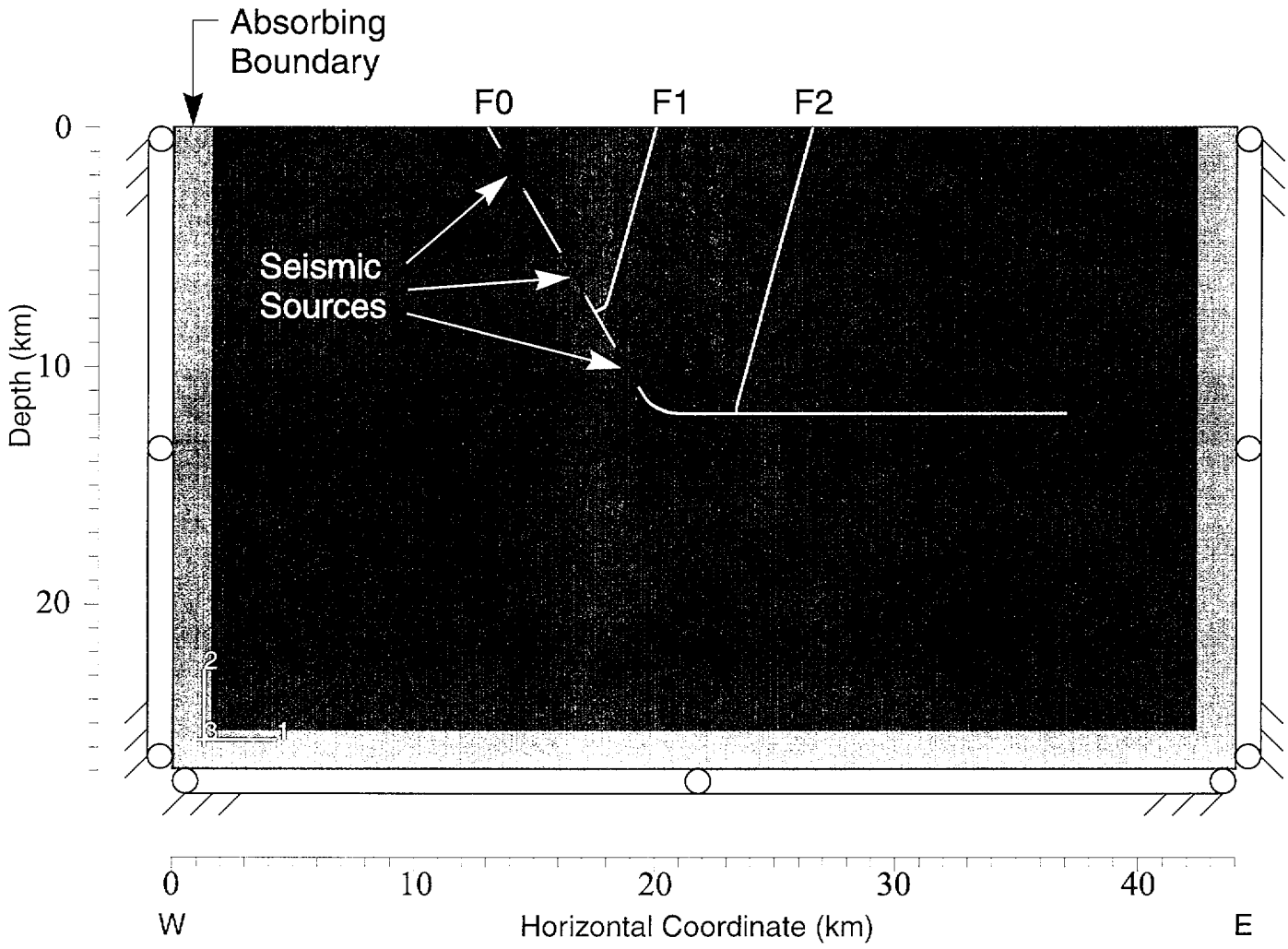
Absorbing
Boundary
F0
F1
F2
Seismic
Sources
Depth (km)
0
10
20
2
3
1
0
10
20
30
40
W
Horizontal Coordinate (km)
E

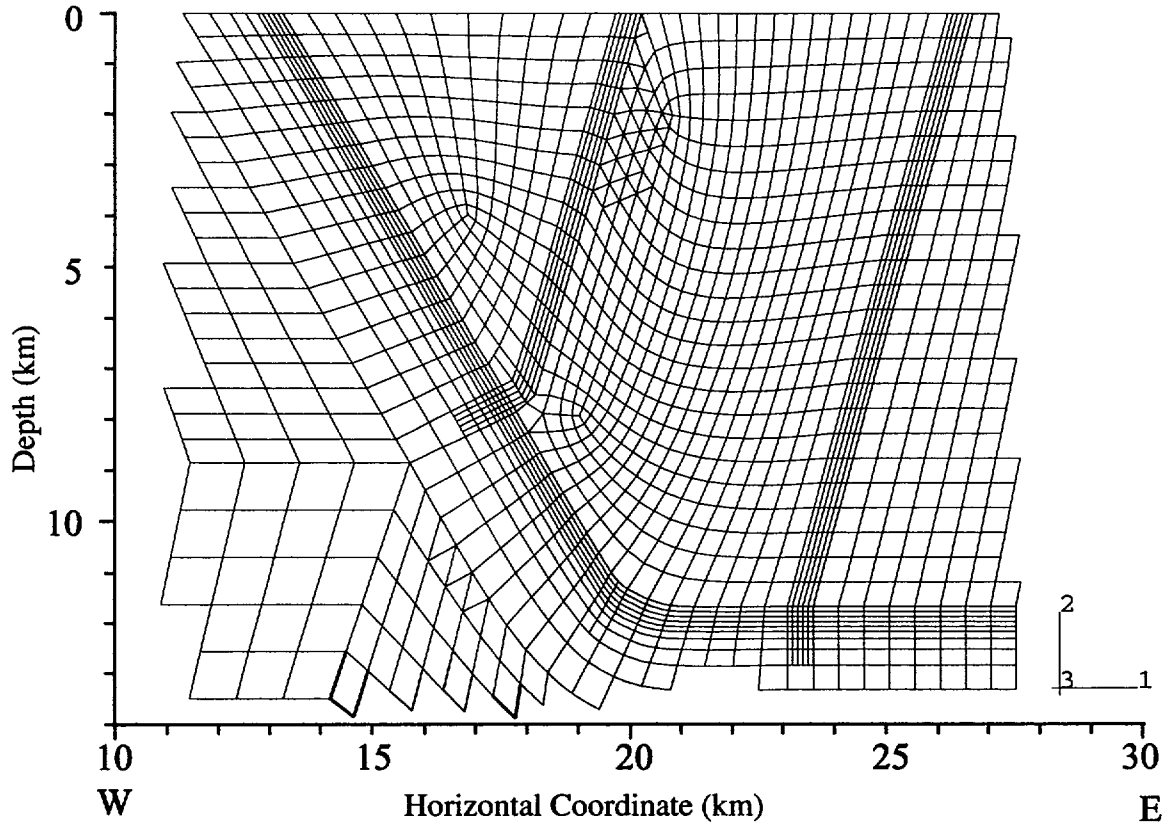
0
5
10
Depth (km)
10
15
20
25
30
W
Horizontal Coordinate (km)
E
2
3
1

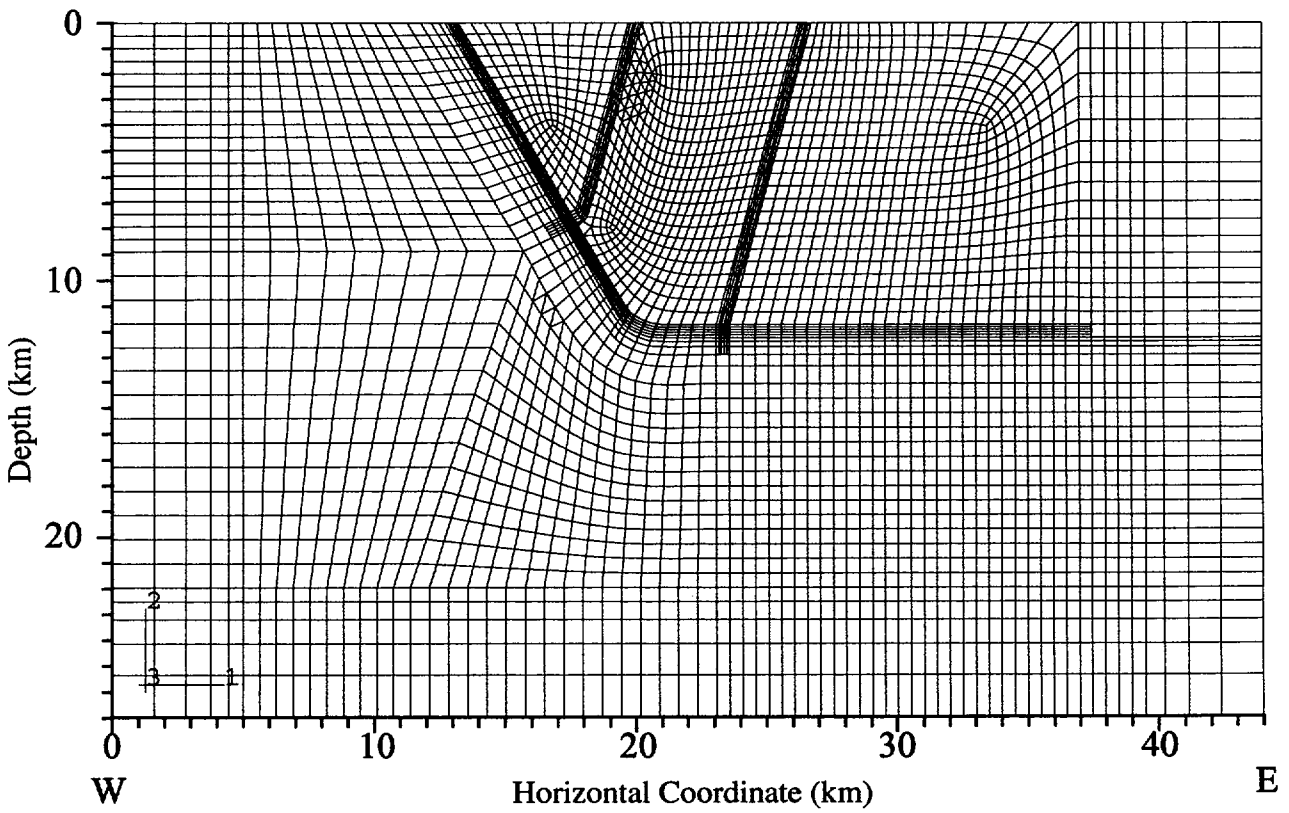
0
10
20
Depth (km)
0
10
20
30
40
W
Horizontal Coordinate (km)
E
2
3
1

Fig 2

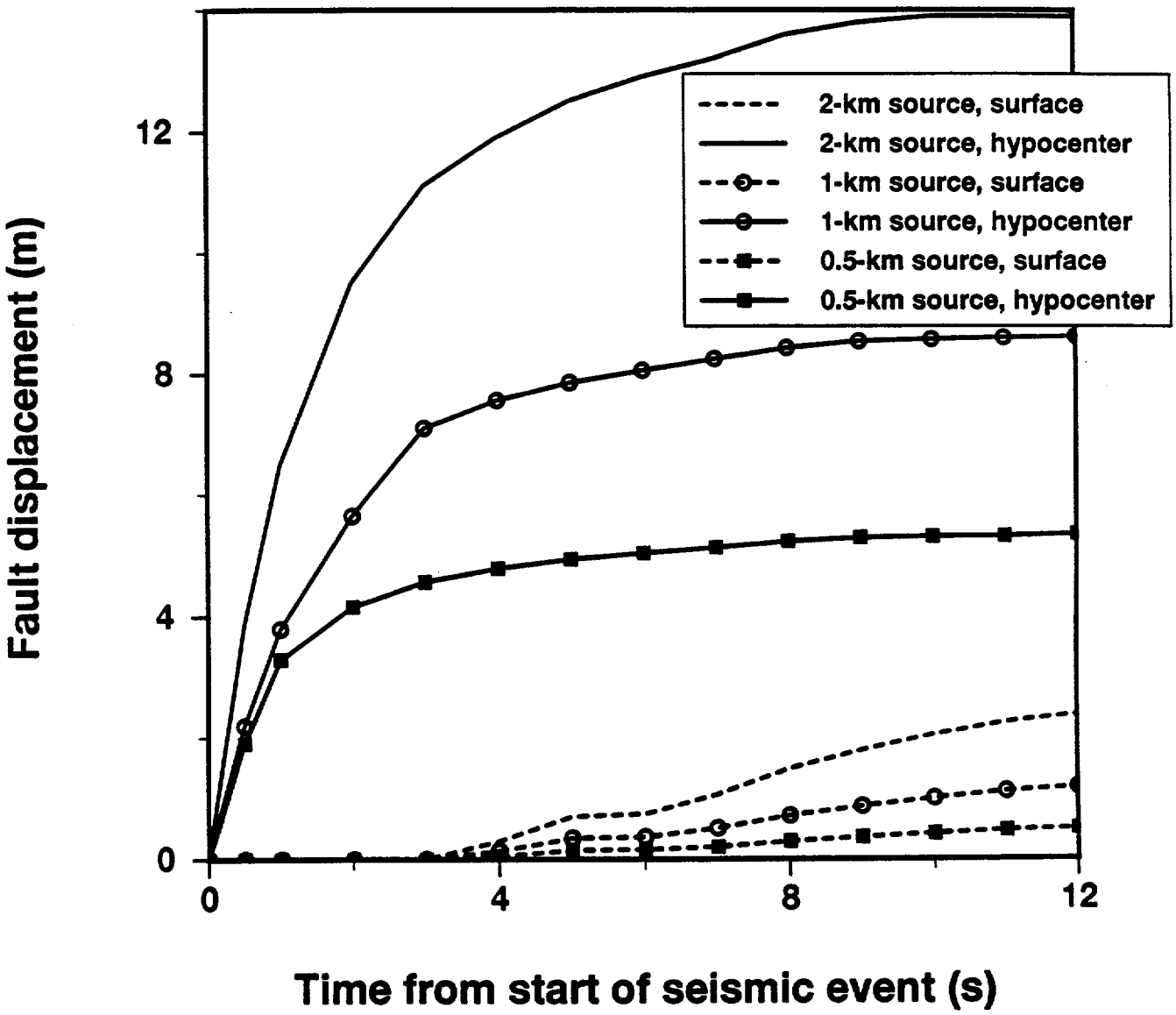
2-km source, surface
2-km source, hypocenter
1-km source, surface
1-km source, hypocenter
0.5-km source, surface
0.5-km source, hypocenter
Fault displacement (m)
0
4
8
12
0
4
8
12
Time from start of seismic event (s)

Fig 3
~~Fig 2~~

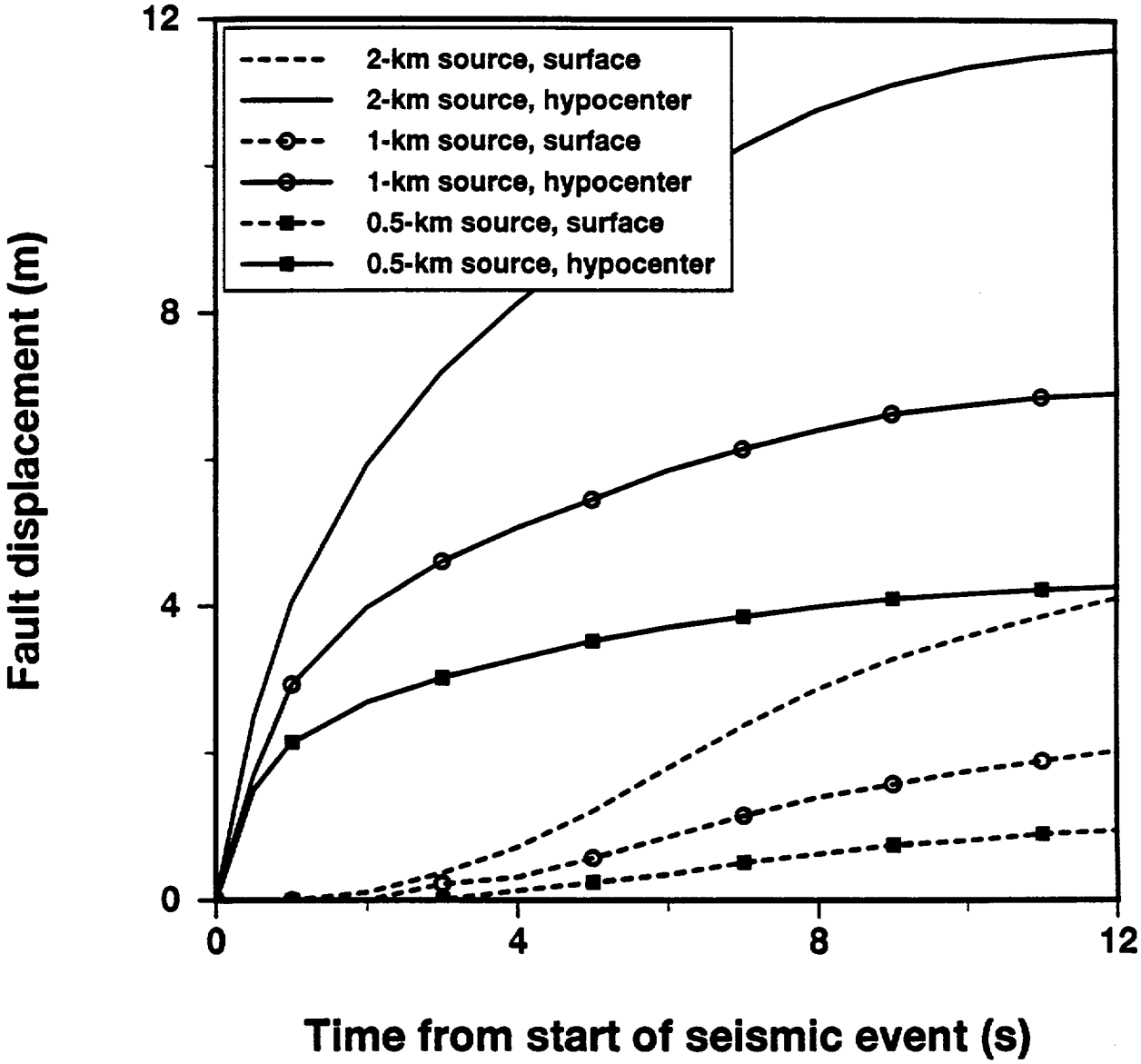
12
8
4
0
0
4
8
12
2-km source, surface
2-km source, hypocenter
1-km source, surface
1-km source, hypocenter
0.5-km source, surface
0.5-km source, hypocenter
Fault displacement (m)
Time from start of seismic event (s)

Fig 4
~~Fig 3~~

1.5 km Depth

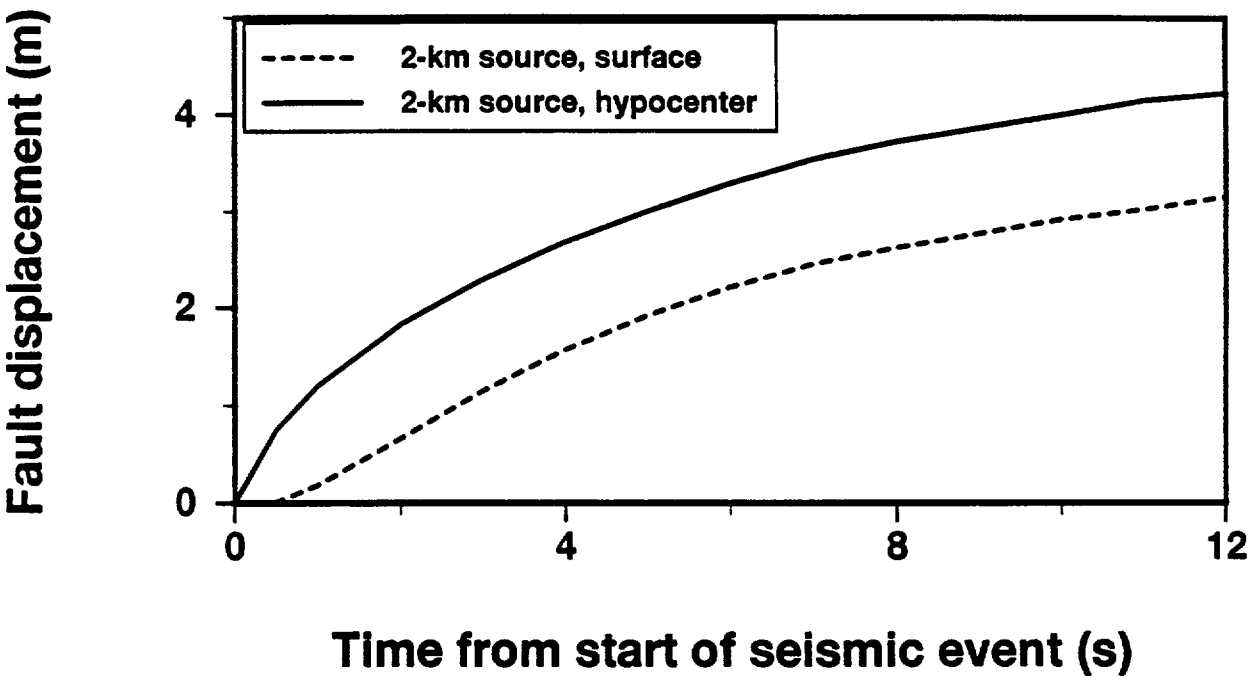

Fig 5
~~Fig 4~~

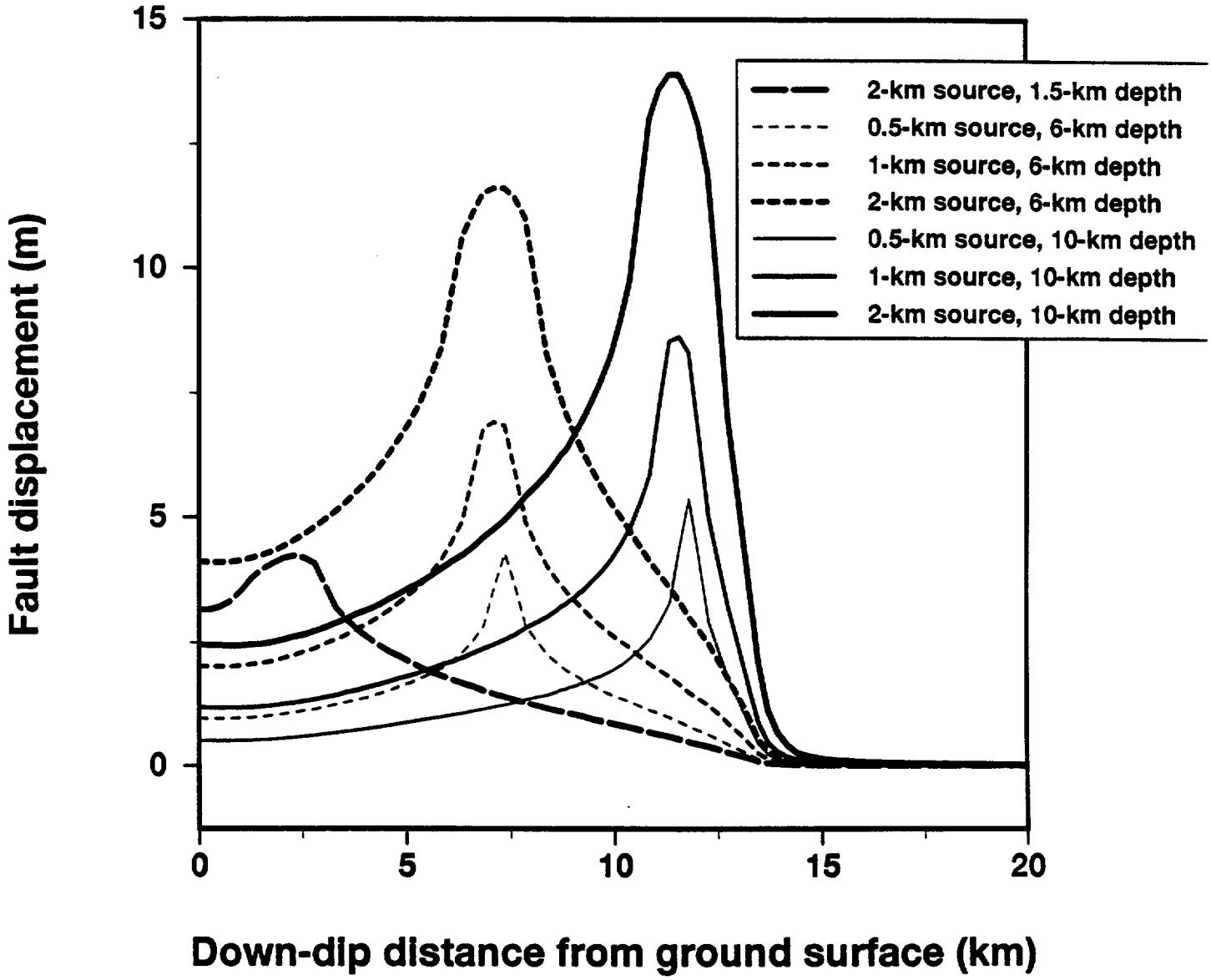
15
10
5
0
0
5
10
15
20
Fault displacement (m)
Down-dip distance from ground surface (km)
2-km source, 1.5-km depth
0.5-km source, 6-km depth
1-km source, 6-km depth
2-km source, 6-km depth
0.5-km source, 10-km depth
1-km source, 10-km depth
2-km source, 10-km depth

Fig 6
~~Fig 5~~

2-km source at 10-km depth

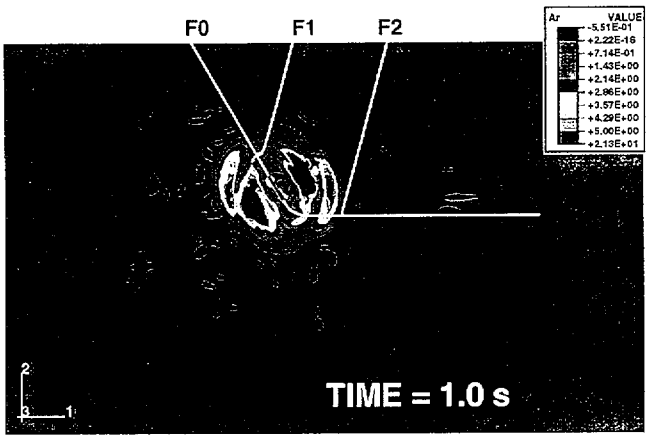

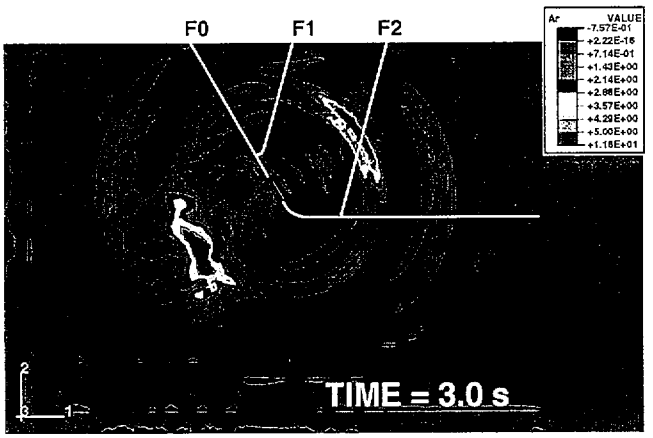

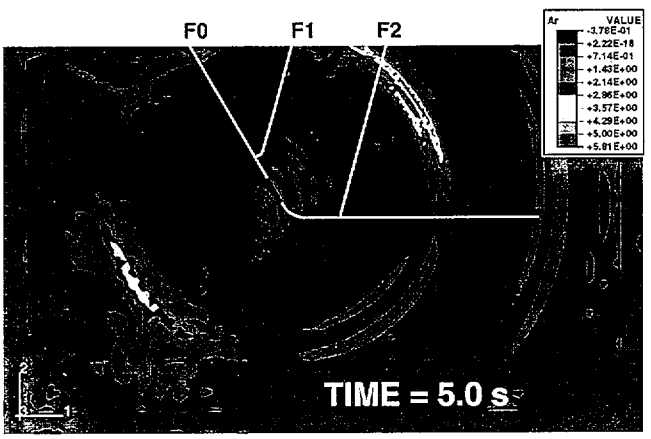

0.5-km source at 10-km depth

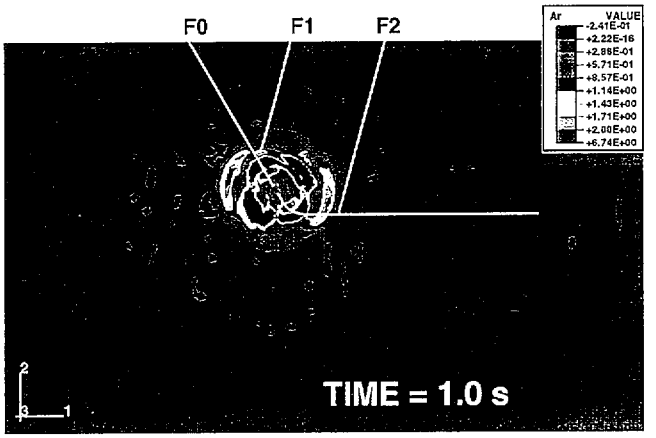

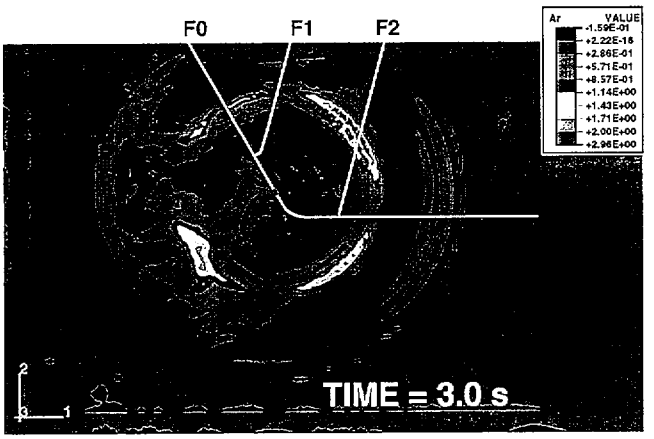

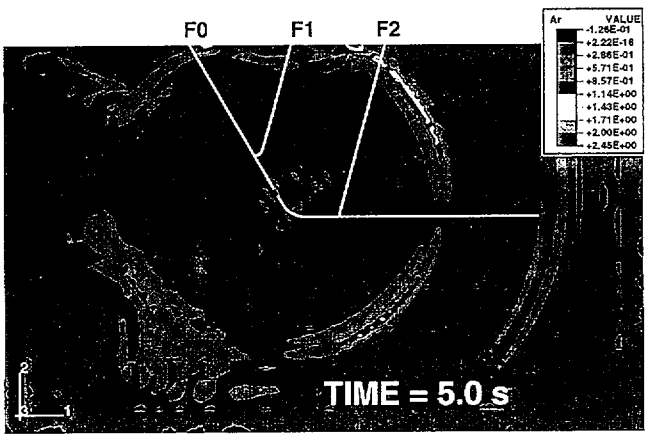

10 km

Horizontal acceleration

Vertical acceleration

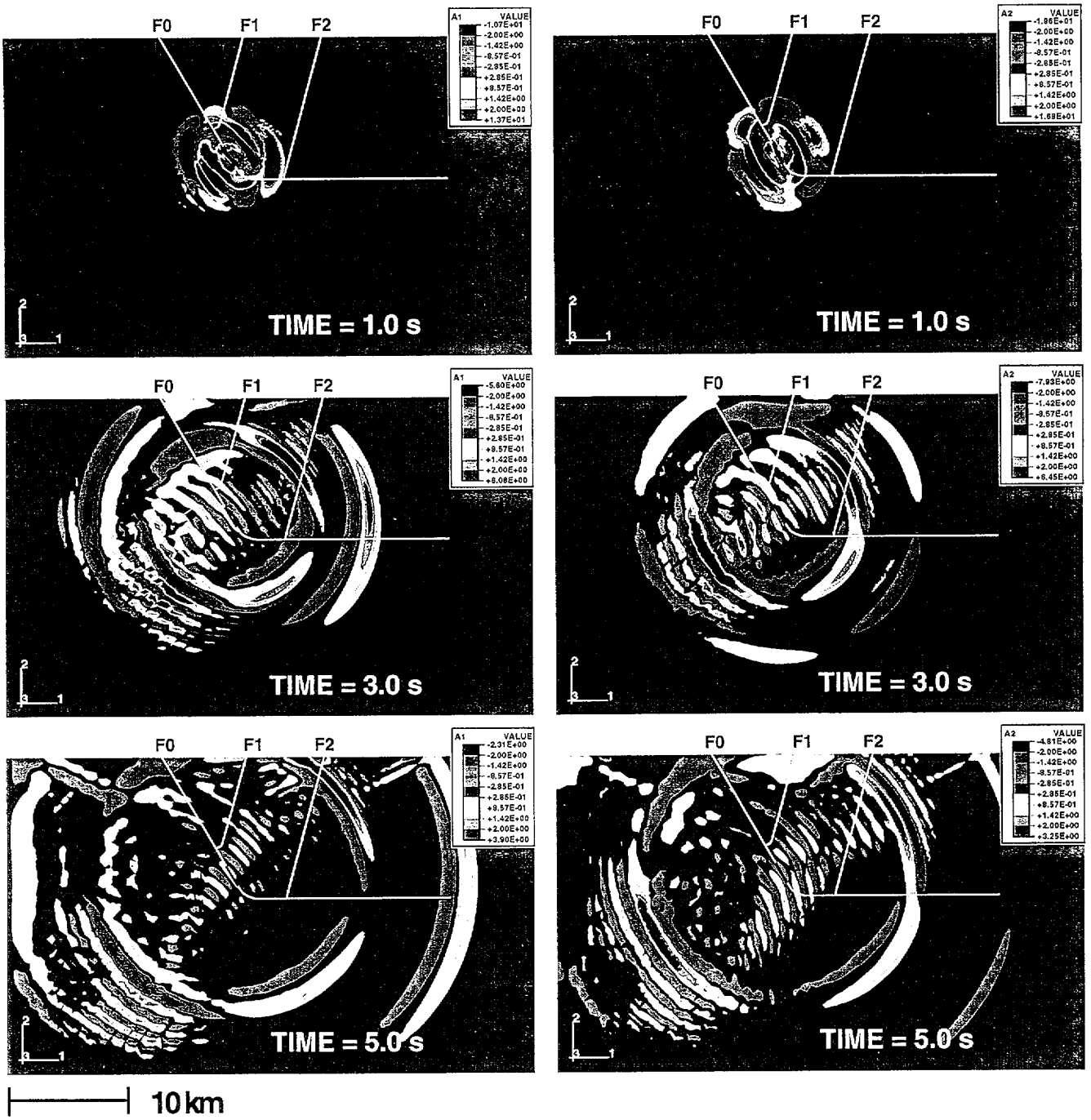

Fig 7

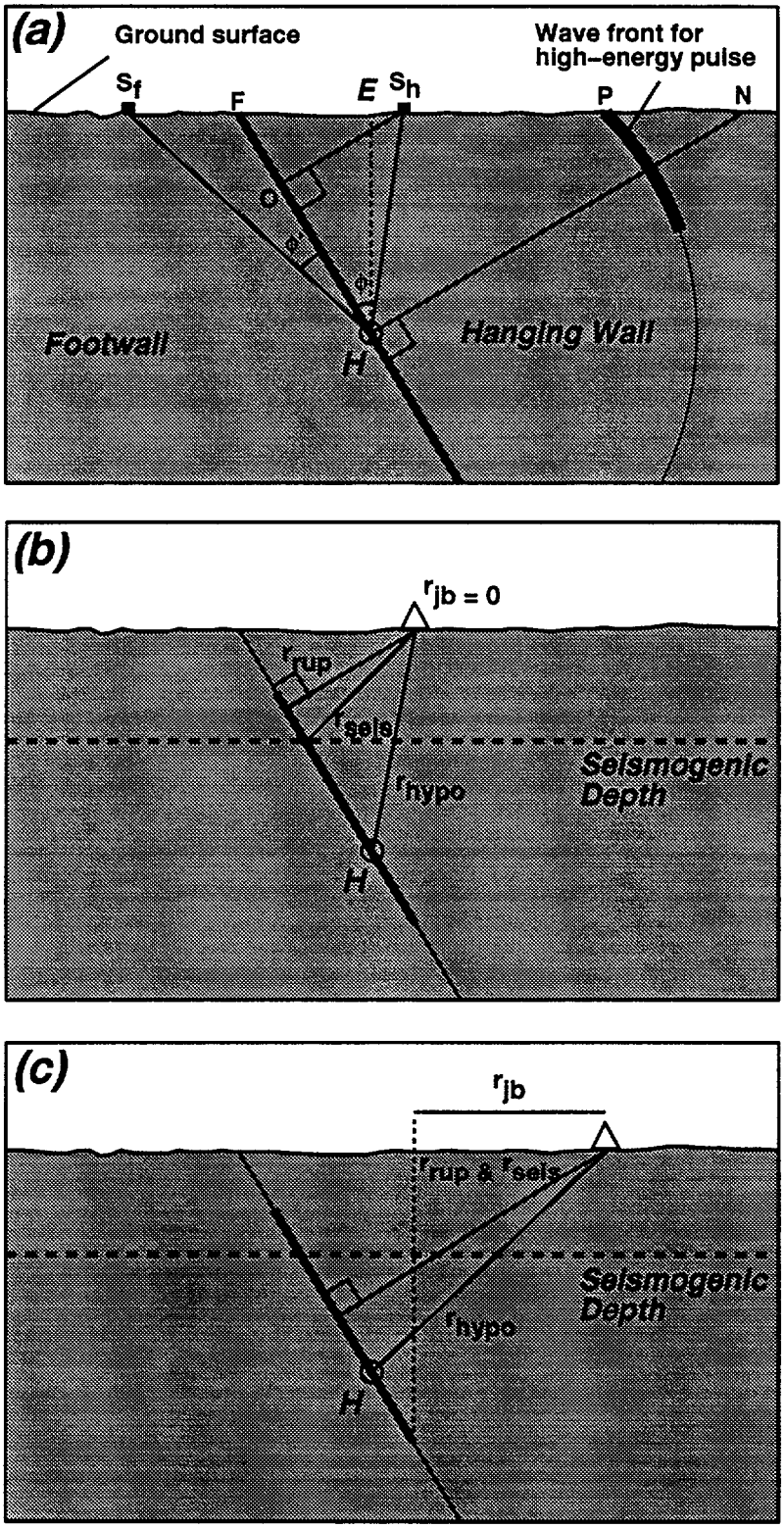

Ofoegbu, Ferrill, Smart, and Stamatakos
Figure 8.

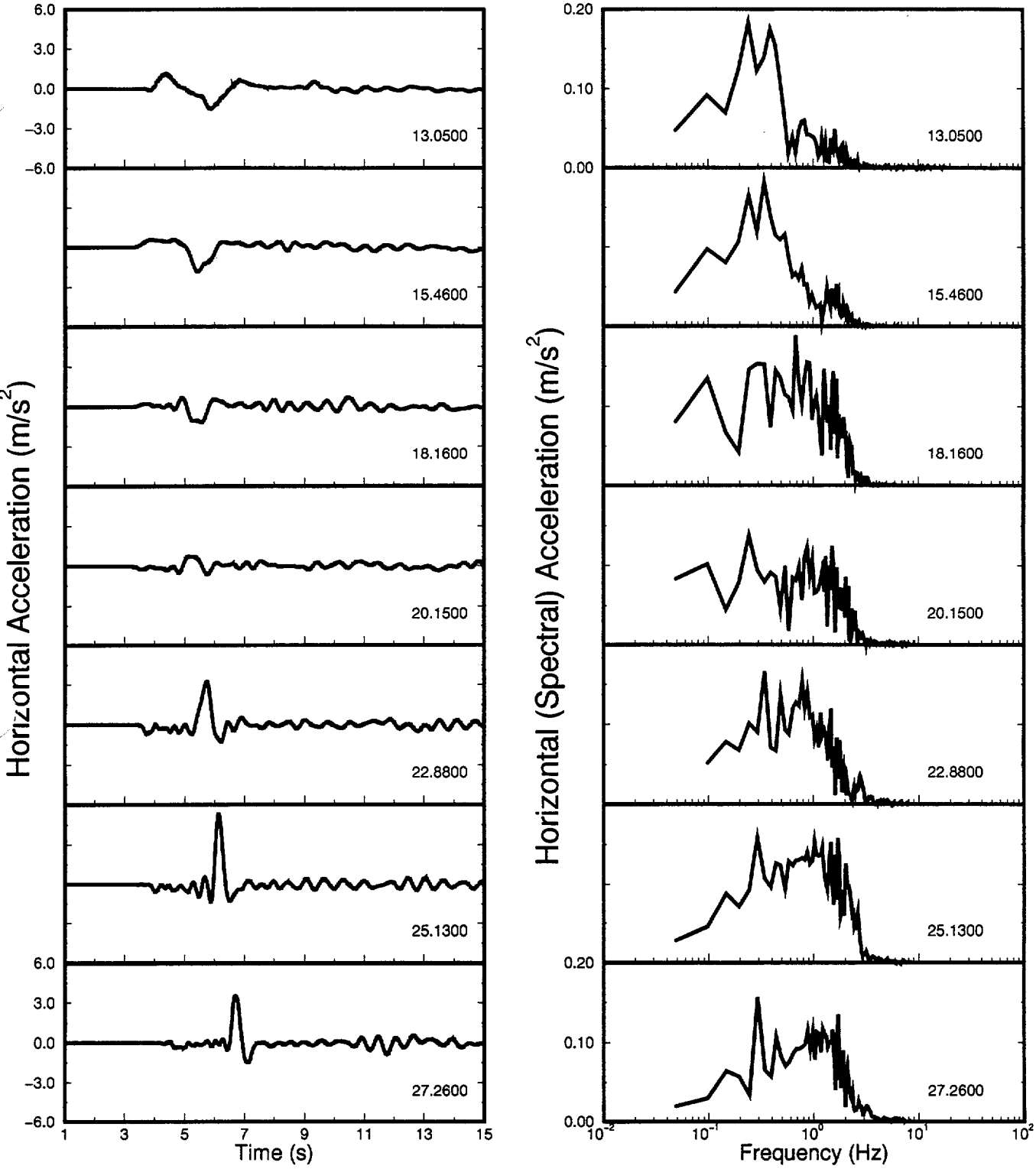
Horizontal Acceleration (m/s^2)
Time (s)
13.0500
15.4600
18.1600
20.1500
22.8800
25.1300
27.2600
Horizontal (Spectral) Acceleration (m/s^2)
Frequency (Hz)

~~to~~ Fig 10

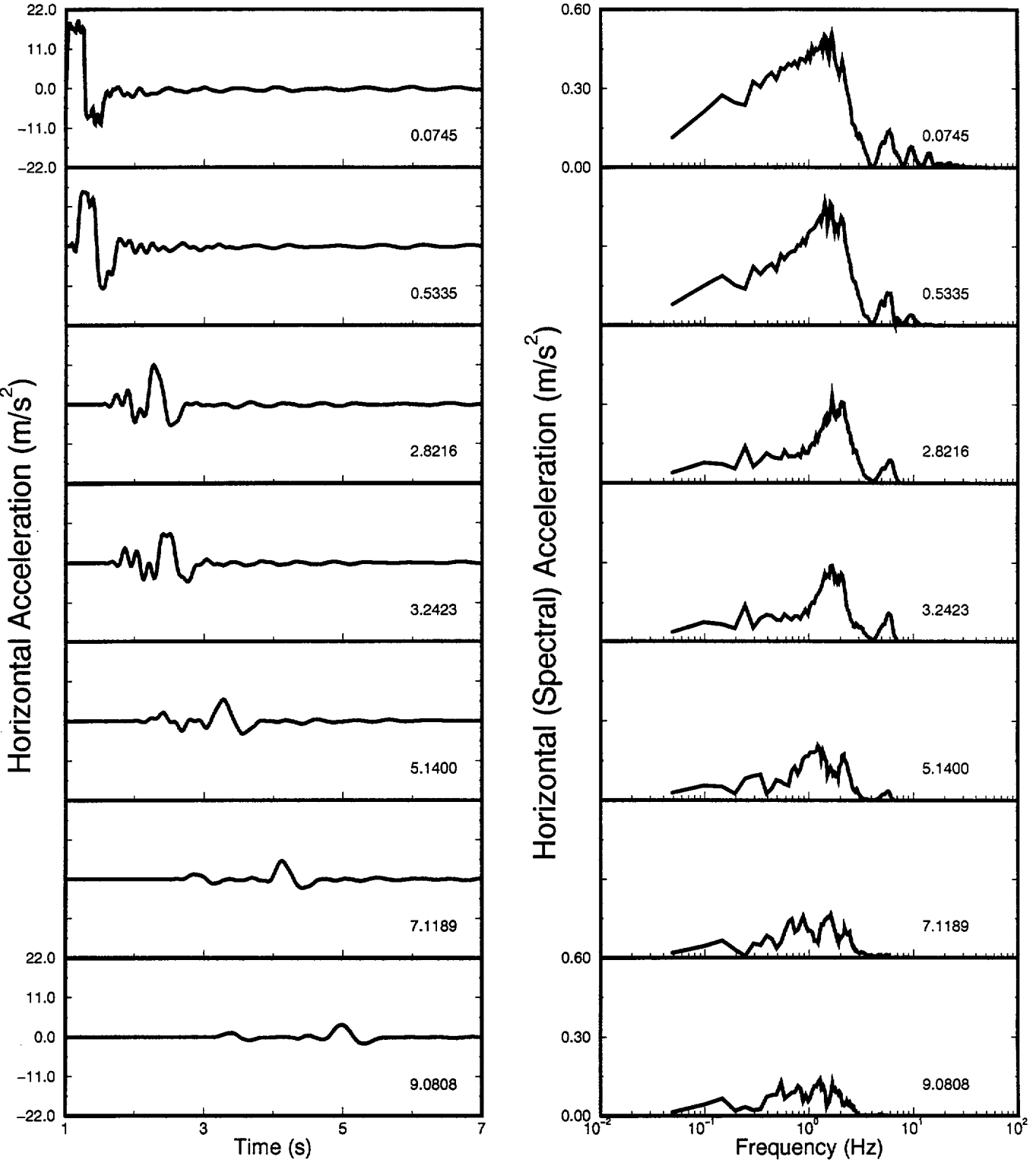
Horizontal Acceleration (m/s^2)
22.0
11.0
0.0
-11.0
-22.0
0.0745
0.5335
2.8216
3.2423
5.1400
7.1189
9.0808
1
3
5
7
Time (s)
Horizontal (Spectral) Acceleration (m/s^2)
0.60
0.30
0.00
10^{-2}
10^{-1}
10^{0}
10^{1}
10^{2}
Frequency (Hz)

Fig 11 B

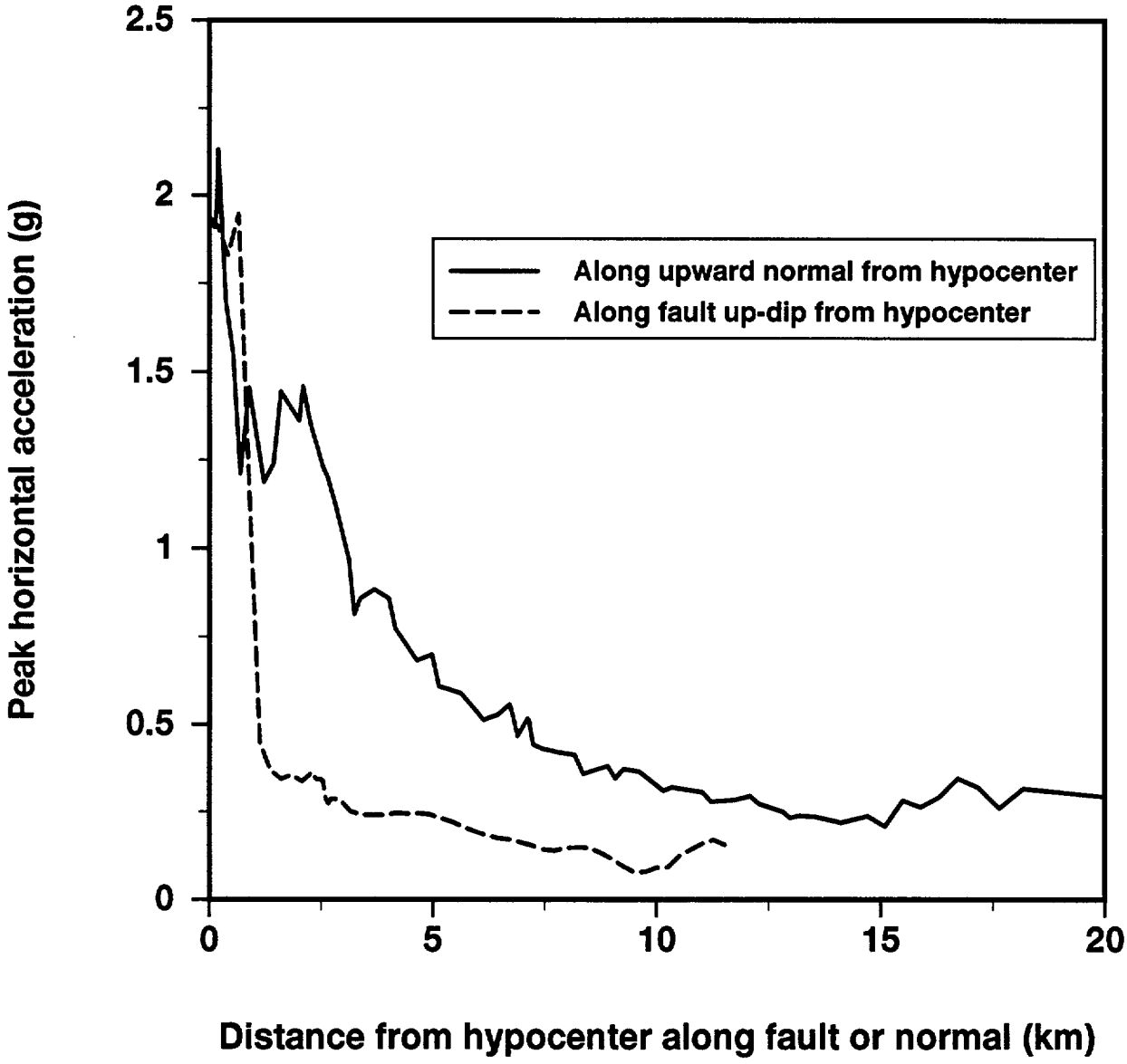
2.5
2
1.5
1
0.5
0
0
5
10
15
20
Peak horizontal acceleration (g)
Distance from hypocenter along fault or normal (km)
Along upward normal from hypocenter
Along fault up-dip from hypocenter

Fig 12

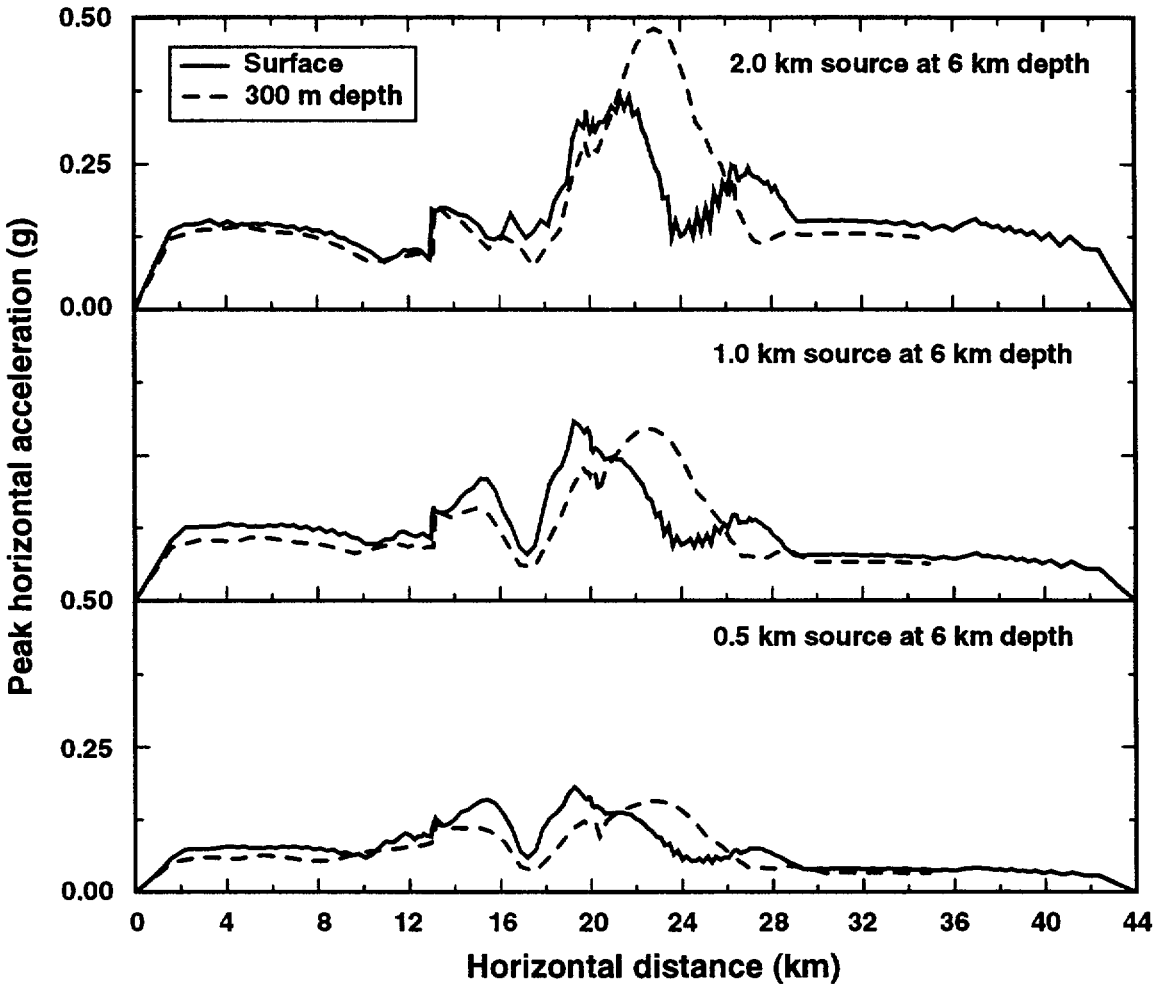
Surface
300 m depth
2.0 km source at 6 km depth
1.0 km source at 6 km depth
0.5 km source at 6 km depth
Peak horizontal acceleration (g)
0.50
0.25
0.00
0.50
0.25
0.00
0
4
8
12
16
20
24
28
32
36
40
44
Horizontal distance (km)

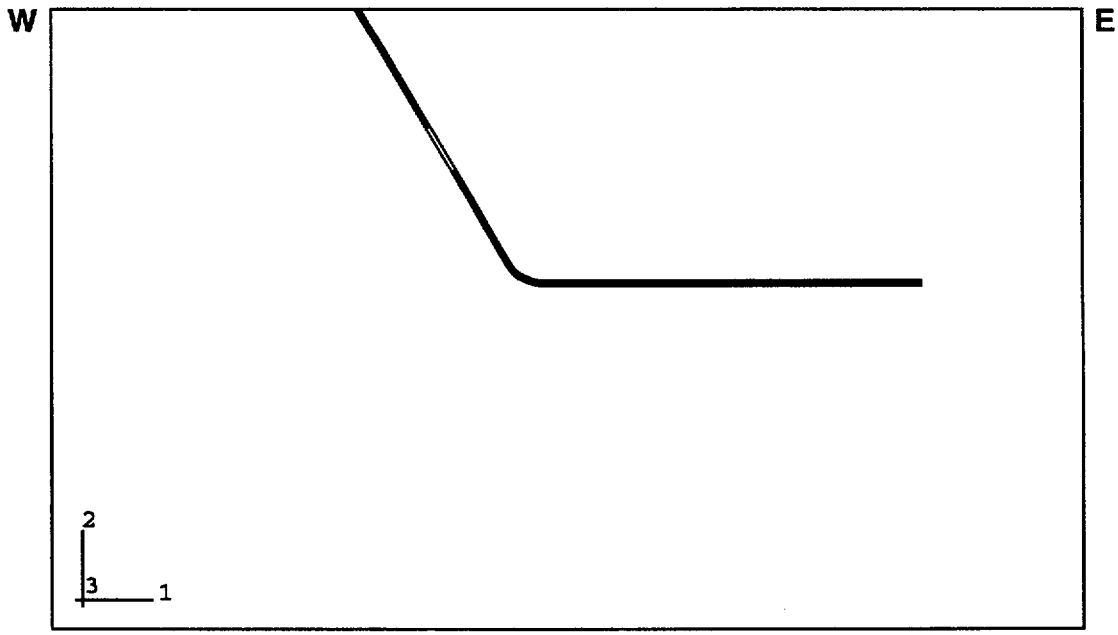
W
E
2
3
1

13
Fig ~~12~~

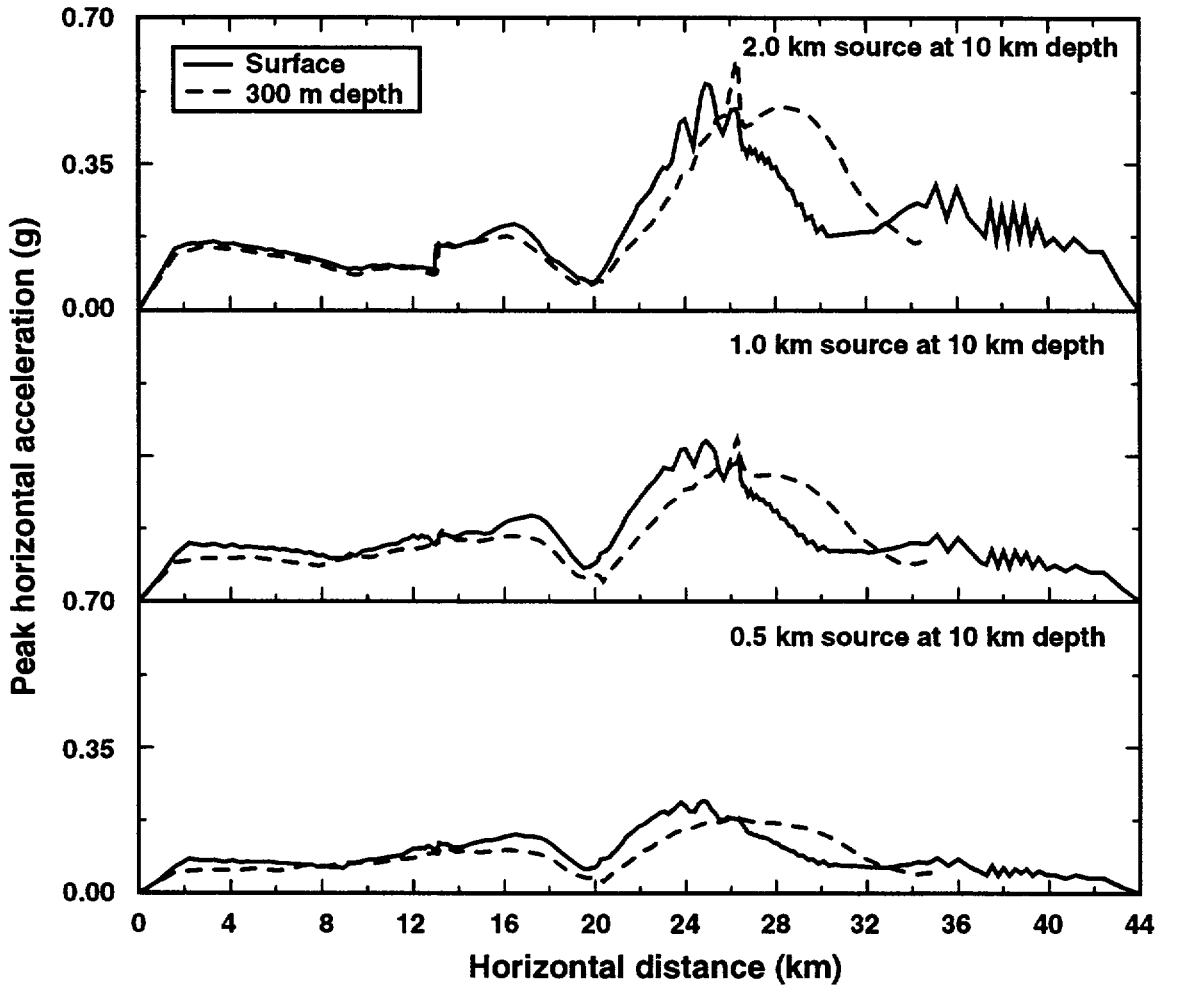
Surface
300 m depth
2.0 km source at 10 km depth
1.0 km source at 10 km depth
0.5 km source at 10 km depth
Peak horizontal acceleration (g)
0.70
0.35
0.00
0.70
0.35
0.00
0
4
8
12
16
20
24
28
32
36
40
44
Horizontal distance (km)

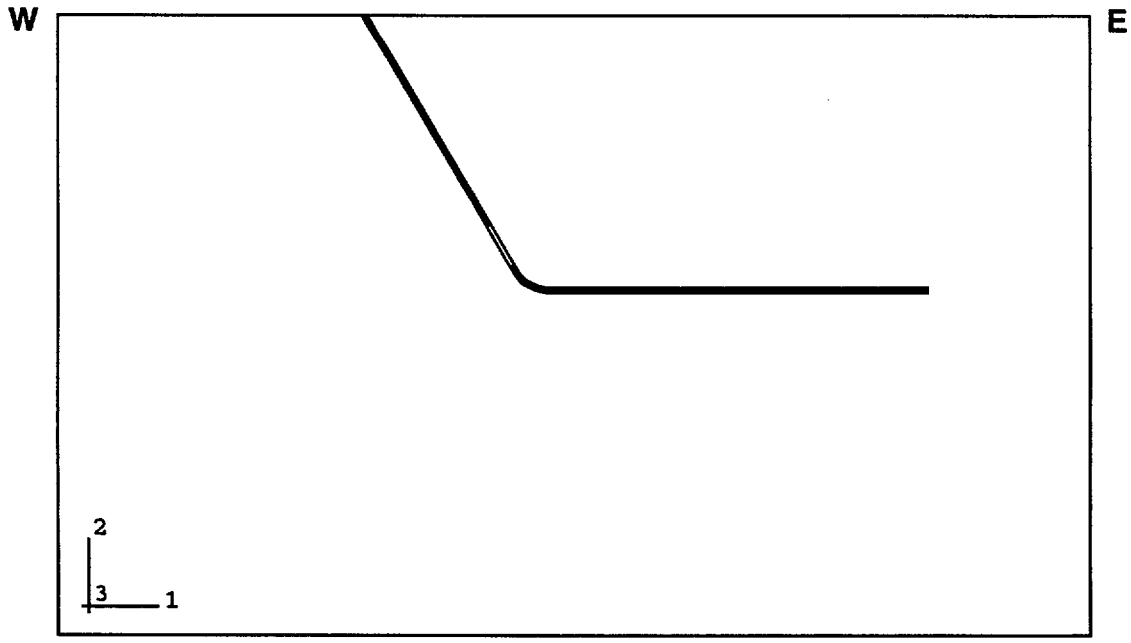
W
E
2
3
1

Fig 14 ~~13~~

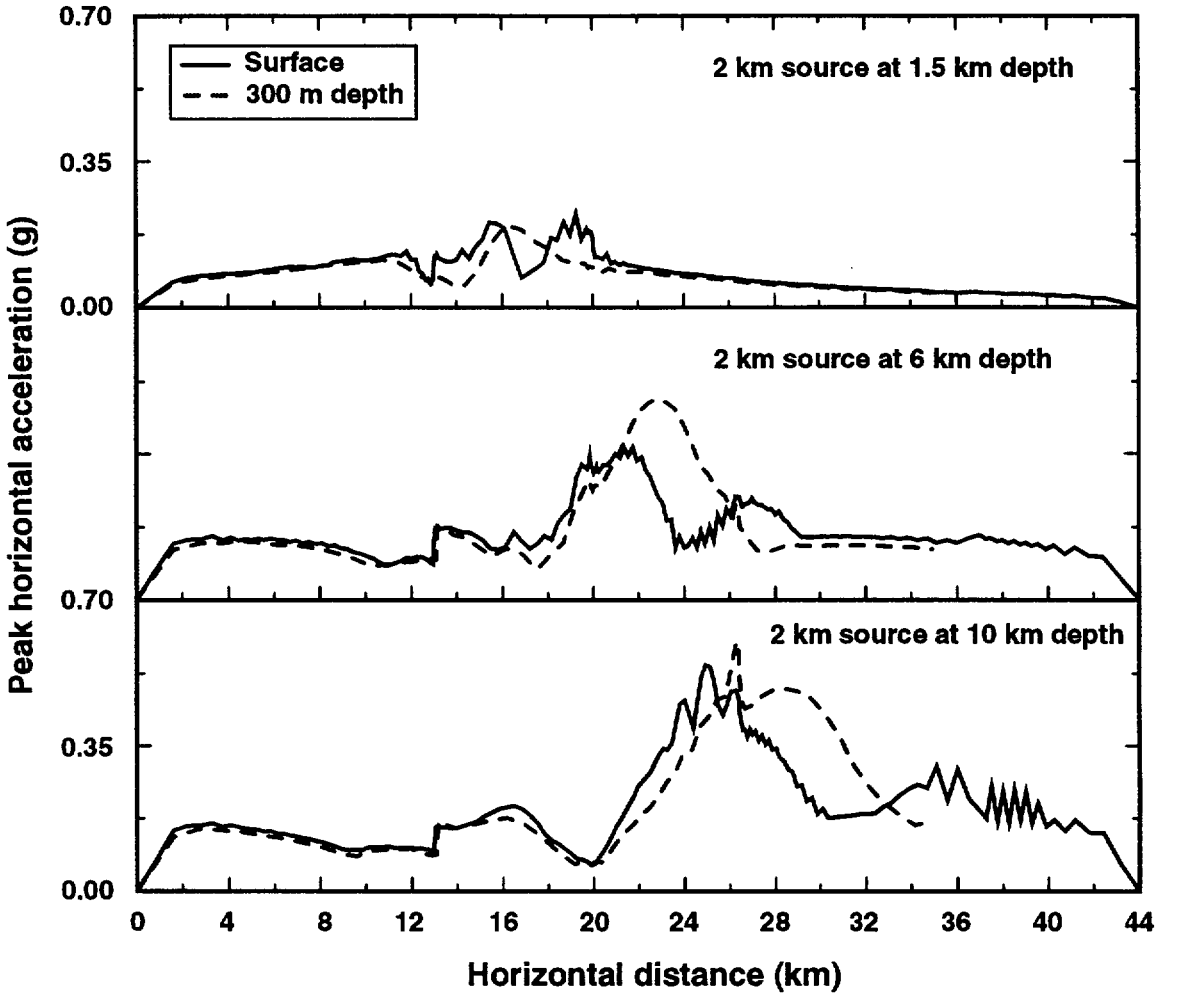
Surface
300 m depth
2 km source at 1.5 km depth
2 km source at 6 km depth
2 km source at 10 km depth
Peak horizontal acceleration (g)
0.70
0.35
0.00
0.70
0.35
0.00
0
4
8
12
16
20
24
28
32
36
40
44
Horizontal distance (km)

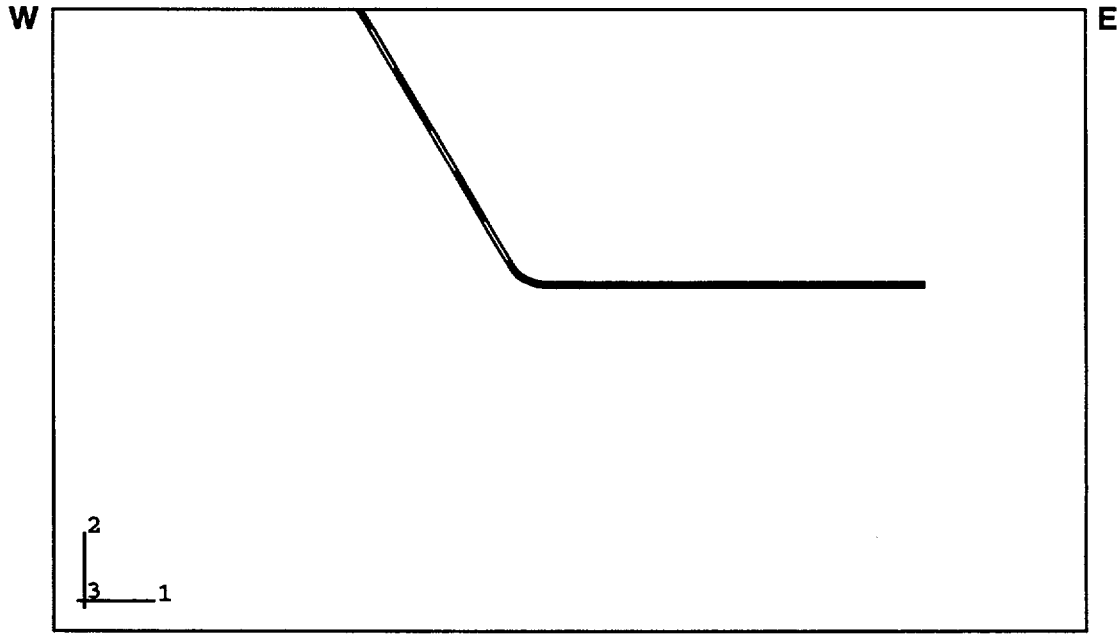
W
E
2
3
1

Fig 15 ~~14~~

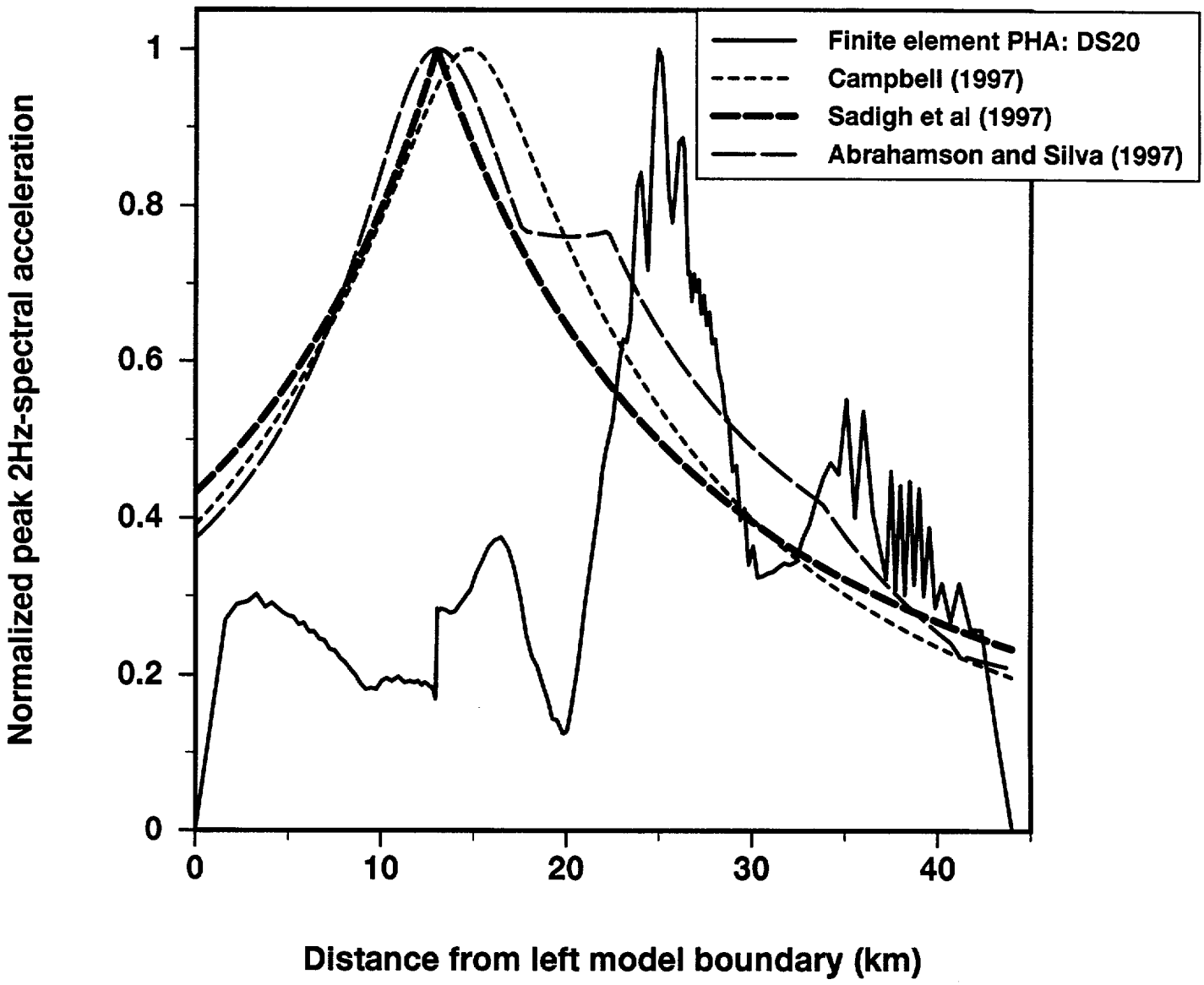
Finite element PHA: DS20
Campbell (1997)
Sadigh et al (1997)
Abrahamson and Silva (1997)
Normalized peak 2Hz-spectral acceleration
1
0.8
0.6
0.4
0.2
0
0
10
20
30
40
Distance from left model boundary (km)

Fig 16(a)

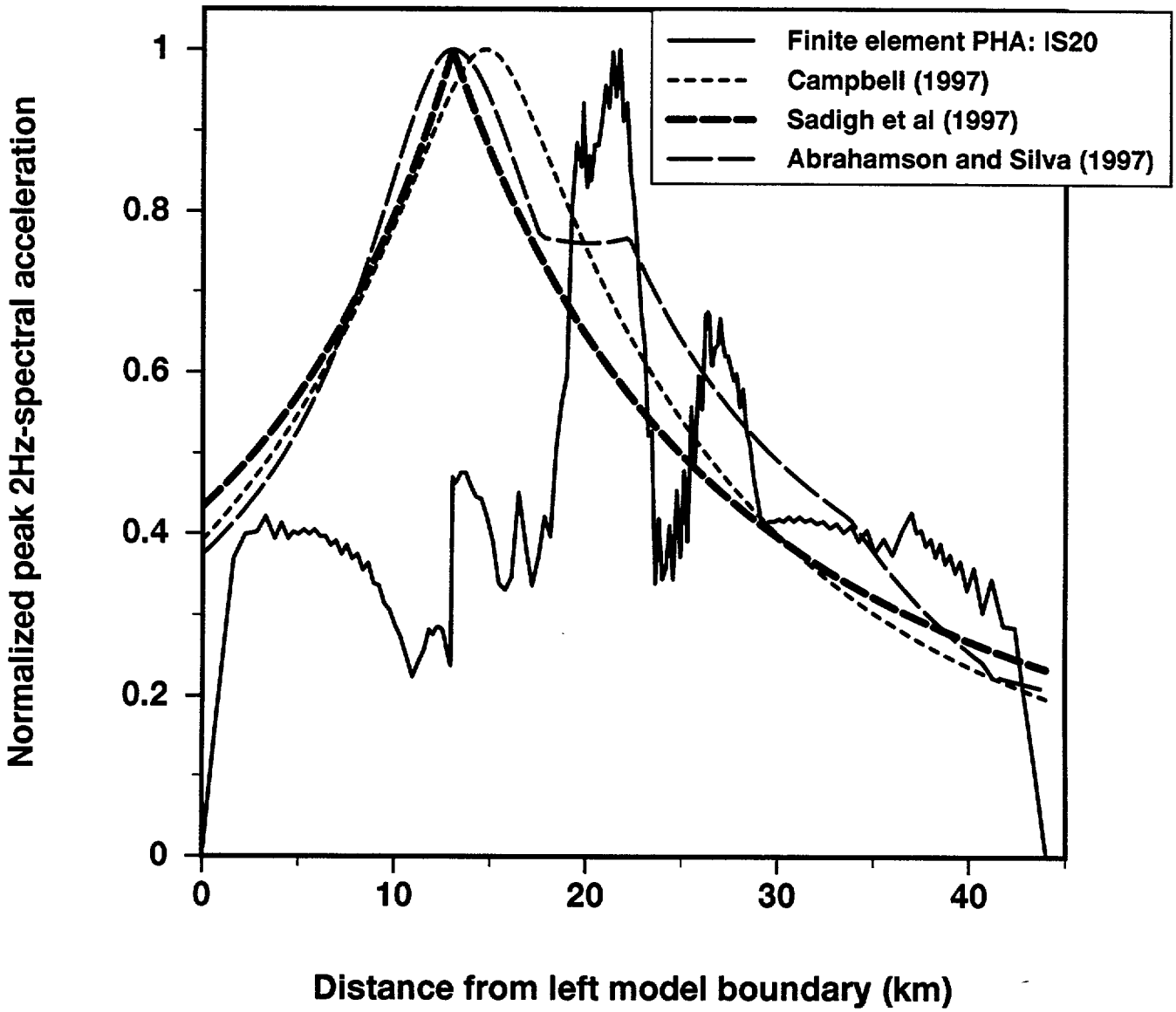
Finite element PHA: IS20
Campbell (1997)
Sadigh et al (1997)
Abrahamson and Silva (1997)
Normalized peak 2Hz-spectral acceleration
1
0.8
0.6
0.4
0.2
0
0
10
20
30
40
Distance from left model boundary (km)

Fig 16(b)

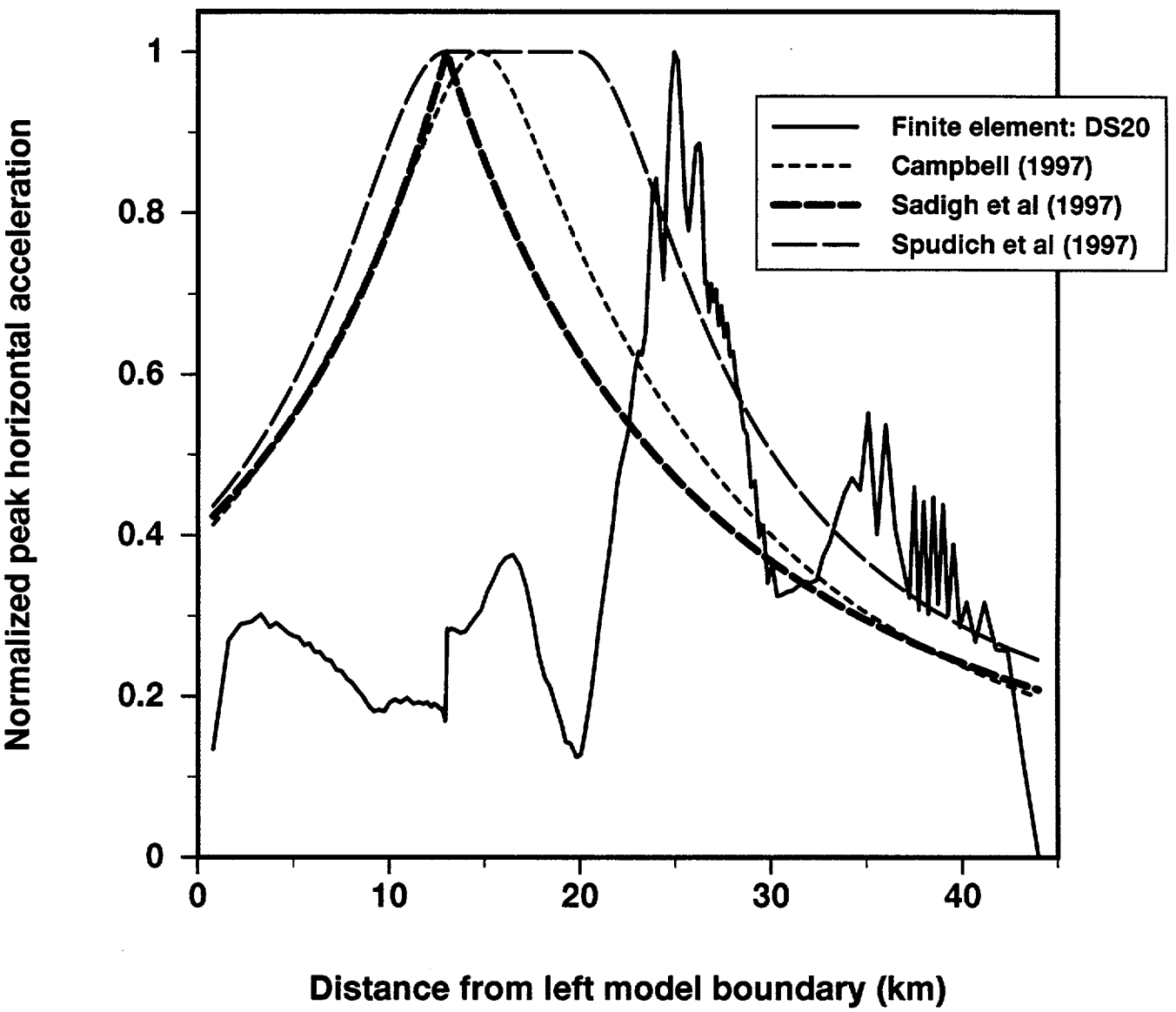
Normalized peak horizontal acceleration
1
0.8
0.6
0.4
0.2
0
0
10
20
30
40
Distance from left model boundary (km)
Finite element: DS20
Campbell (1997)
Sadigh et al (1997)
Spudich et al (1997)

Fig 17(a)

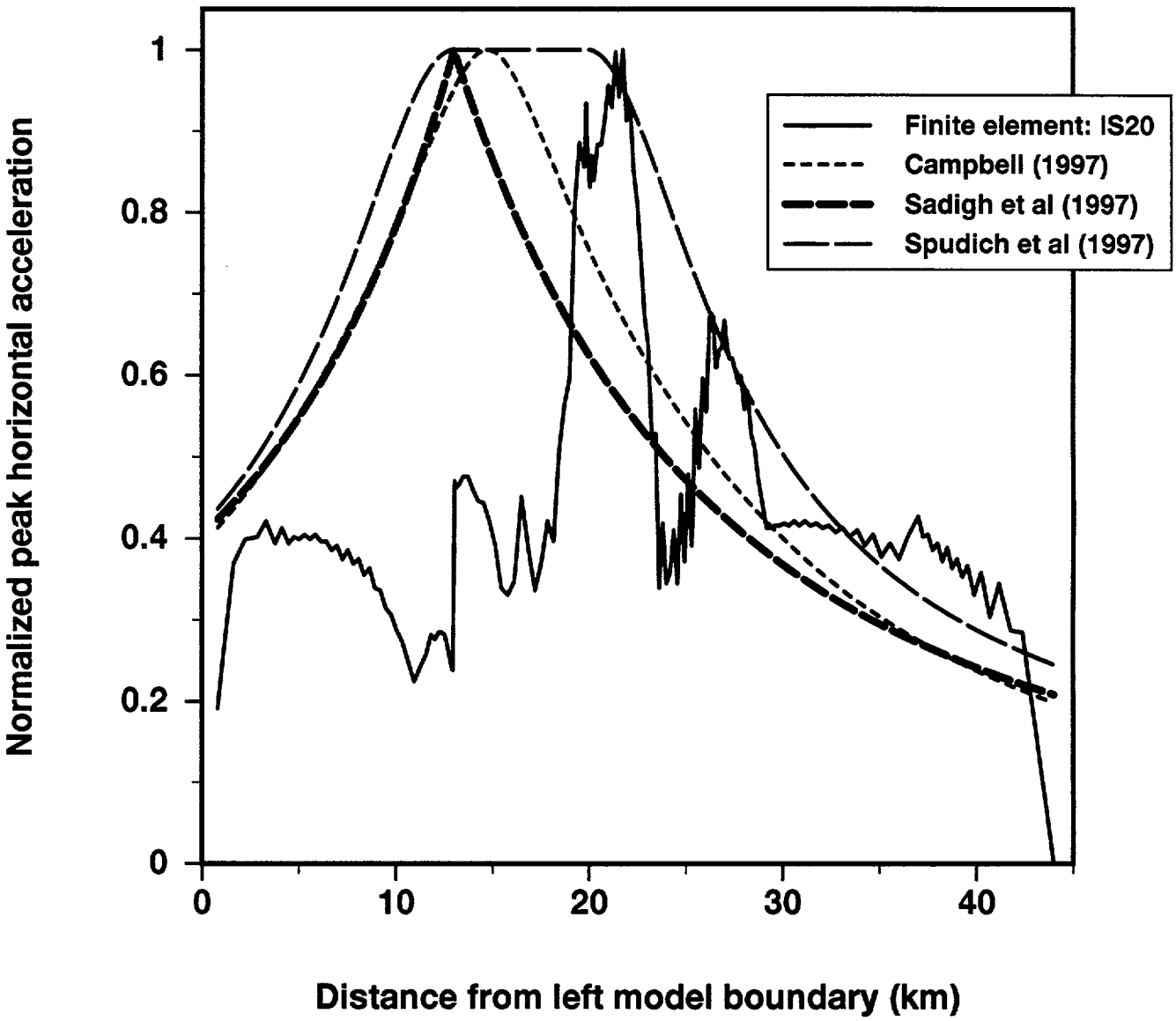
Normalized peak horizontal acceleration
1
0.8
0.6
0.4
0.2
0
0
10
20
30
40
Distance from left model boundary (km)
Finite element: IS20
Campbell (1997)
Sadigh et al (1997)
Spudich et al (1997)

Fig 17 (b)

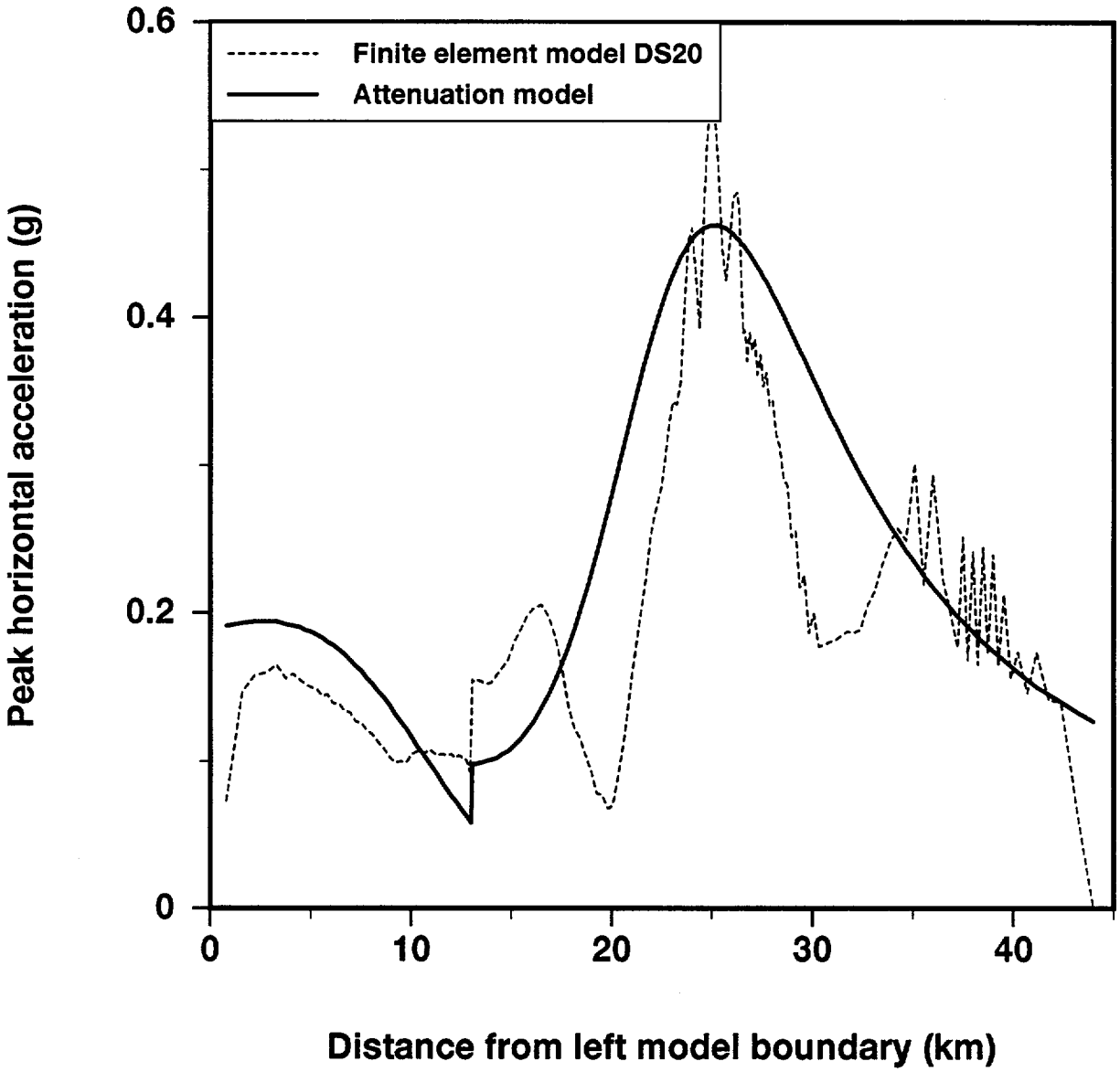
Finite element model DS20
Attenuation model
Peak horizontal acceleration (g)
0.6
0.4
0.2
0
0
10
20
30
40
Distance from left model boundary (km)

18

Fig ~~16~~

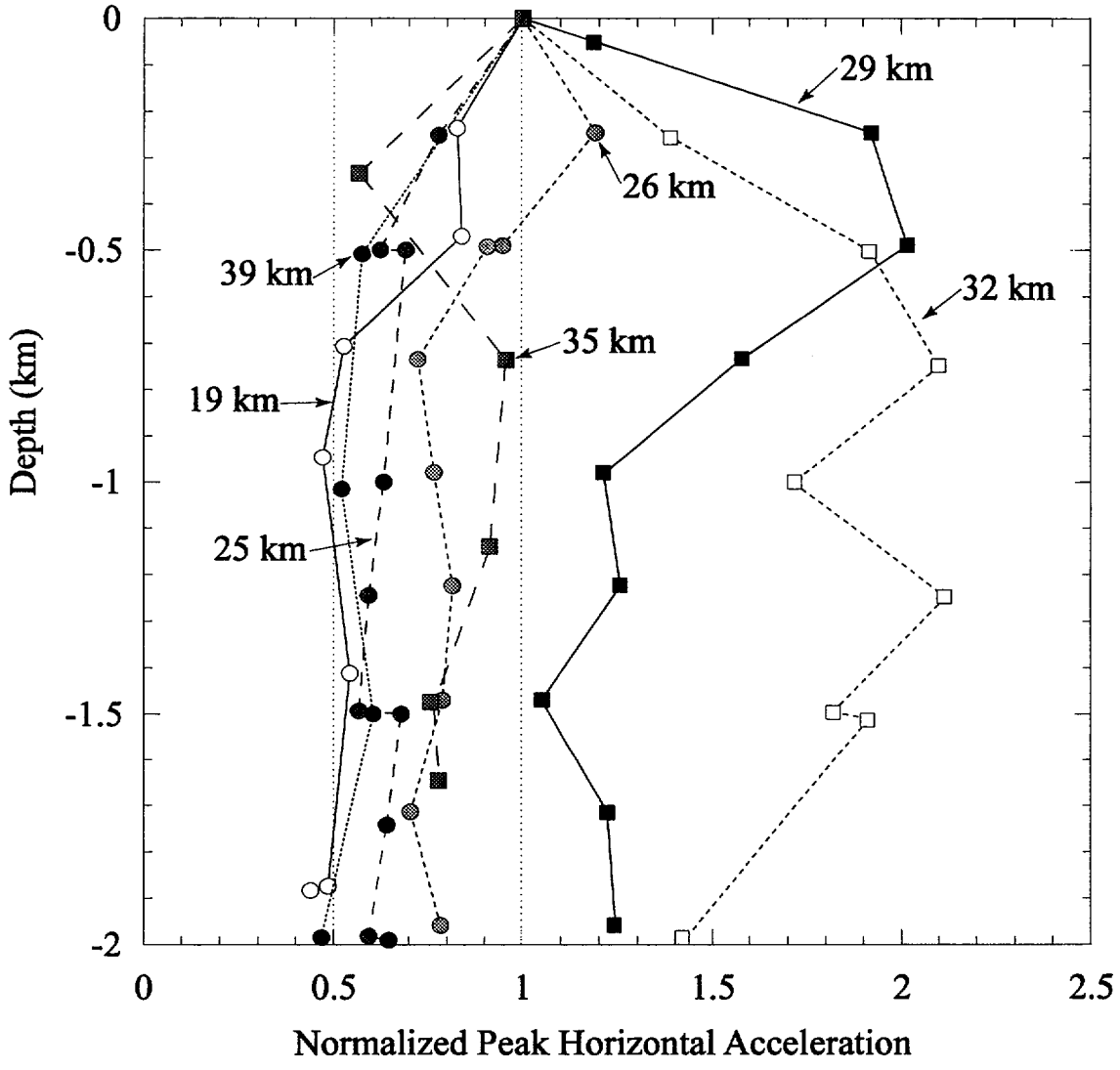
0
-0.5
-1
-1.5
-2
Depth (km)
0
0.5
1
1.5
2
2.5
Normalized Peak Horizontal Acceleration
29 km
26 km
39 km
32 km
35 km
19 km
25 km

Fig 19